

STUDIES OF THE LOW TEMPERATURE BEHAVIOUR OF CoNb_2O_6

STUDIES OF THE LOW TEMPERATURE BEHAVIOUR OF
 CoNb_2O_6

By

TIMOTHY JOHN SAGAN MUNSIE, B.A.SC. (HONS. SPEC.)

A Thesis

Submitted to the School of Graduate Studies

in Partial Fulfilment of the Requirements

for the Degree

Master of Science

McMaster University

©Copyright by Timothy Munsie, October 2012

MASTER OF SCIENCE (2012)
(Department of Physics and Astronomy)

McMaster University
Hamilton, Ontario

TITLE: Studies of the Low Temperature Behaviour of CoNb_2O_6

AUTHOR: Timothy Munsie, B.A.Sc. (Hons. Spec.)

SUPERVISOR: Graeme M. Luke

NUMBER OF PAGES: xiv, 100

Abstract

This thesis is the result of several experiments designed to probe the low temperature physics underlying the 1D-Ising-like behaviour of chains of spins in the structure of Cobalt Niobate, CoNb_2O_6 . A collection of prior work has been done by several groups prior to this, focusing on mapping the phase diagram above 0.5K. Interest in this material was renewed recently based upon theoretical work and experimental confirmation of the unique structure of the spins in the system. The bulk of this work was done at temperatures below the previously investigated range to probe the unique properties of this system.

The material was grown at McMaster University using the optical floating zone technique from oxide powders. The crystal was examined and oriented using single crystal and Laue diffraction and was cut for use in further experiments. Squid magnetometry was used to confirm the material properties and phase transition temperatures, and was compared to literature values.

Heat capacity measurements were performed locally down to 2K, and by collaborators at Waterloo in the range from 330mK to 1K. The heat capacity measurement confirmed the 2.9K transition and explored the relaxation time of the material. Cobalt niobate was found to have an exceptionally long relaxation time at low temperatures indicating strong spin-spin interactions. A sharp transition with zero applied field was found to become a broad, smooth feature at 2.9K when a small field was applied.

We performed μSR measurements in zero, longitudinal and transverse field. The μSR results confirmed the long relaxation time found by the heat capac-

ity measurements, which may reflect the coupling of the spin system to the lattice. Additionally, the material was never seen to statically order in zero or longitudinal field down to 700mK and up to 1T. The material was found to behave dynamically throughout all the field ranges.

Acknowledgements

This is the end of one chapter of a journey that was started almost a decade ago. The first person I really need to thank is Dr. R. H. Prince from York University. He was the founder of the Engineering program there, and more importantly someone who convinced me that I really belonged in graduate school. The combined efforts of Dr. K. Dalnoki-Veress and Dr. A. Sills made it possible for me to gain admission to McMaster for the purpose of obtaining the third and fourth year courses that I would require to be successful at graduate studies in Physics, so to them I owe a debt of gratitude.

Dr. H. Dabkowska, Dr. A. Dabkowski and Dr. P. Dube have all made me a far more competent researcher, far more knowledgeable about crystal growth, sample preparation, characterization and experimentation in general. Had it not been for continued conversations I would have ended up far more lost in the academic wilderness. Most importantly I count them all as friends.

This project would not have been nearly as successful if not for the efforts in the crystal growth lab of Ms. C. Marjerrison and, especially, Ms. A. Kinross with whom I worked extensively on the run up for this material. I am privileged to say was able to adopt as the topic for my Masters Thesis the USRA project that she began. Ms. Kinross' contribution to this work cannot be understated.

If it was not for the efforts of Mr. T.J. Williams I do not believe that I would have ever understood μ SR, which I still consider a personal work in progress, or have been nearly as successful. His company on this journey has been invaluable, both academically and personally. Most importantly, whenever I feel that I am not doing enough, or that I do not know enough, he always reminds me that I am, and I do and to press on.

If it was not for the constant support of my family, and in particular my younger sister, Dr. L.N. Munsie, this journey would not have happened, and if it had, if not for her I do not know if I would have applied to McMaster. I still do not believe that there is as comprehensive a condensed matter department in Canada, and I feel continually stimulated by everything that can be done, and is done, in the department. Further, I also do not believe that I will ever be able to live down losing the family 'Doctor Race', especially not to Lise.

And the final and most important acknowledgement I have goes to Dr. G.M. Luke. All I can say is that I glad he saw something in me, and I can only hope to live up to that. The opportunities that I have gotten from working with him, and the academic latitude that he lets me explore is exactly what I needed in a supervisor to succeed. He gives me just enough rope to hang myself and stops me before I get almost far enough off track to use it. To quantify the amount that I have learned is such a short time would be a task better fit to the Astronomy half of the department, but I feel that there is still so much more for me to learn. I am glad to have such a guide to help me to my future successes.

~T.J.S. Munsie

Co-Authorship

All of the projects discussed in this thesis are collaborative efforts.

The CoNb_2O_6 crystal discussed in this thesis were grown primarily by myself, Dr. H. Dabkowska and Ms. A. Kinross as part of her summer undergraduate student research award. The initial characterization and cutting of this crystal was done predominantly by Dr. A. Dabkowski, Dr. P. Dube and Ms. A. Kinross. The Laue diffraction, SQUID magnetometry and further crystal cutting and polishing were performed at McMaster University utilizing the resources of the Brockhouse Institute of Material Research, while alignment and sample preparation at TRIUMF was done by myself. The heat capacity measurements done at McMaster were performed by myself with the help of Dr. P. Dube who was instrumental in both the physical technique and result interpretation. The heat capacity measurements at the lowest temperatures were undertaken by Dr. J. Kycia and Mr. D. Pomaranski at their facilities at the University of Waterloo with samples provided. The μSR experiments were performed at TRIUMF. The creation of the proposal for beamline time and the actual experiment were done by myself, however there were a significant number of collaborators involved: Dr. G.M. Luke; Dr. Y.J. Uemura (Columbia); Dr. S. Dunsiger(Munich); Dr. T. Goko(Columbia); Dr. F. Ning(Columbia/Zhejiang); Mr. T.J. Williams, Ms. A. Kinross, Mr. R. D’Ortenzio, Ms. M.T. Medina, Mr. C. Arguello(Columbia), Mr. L. Liu(Columbia), Mr. J. Xu(Columbia), Mr. B. Fransden (Columbia), Mr. W.C. Chung (Columbia) and Mr. K. Crowley (Columbia).

Finally, the writing herein this thesis is the result of my own work, performed under the guidance of Dr. G.M. Luke, with input from the respective collaborators listed above.

Table of Contents

Abstract	iii
Acknowledgements	v
Co-Authorship	vii
List of Figures	xi
List of Tables	xiii
Chapter 1 Introduction and Theoretical Background	1
1.1 Cobalt Niobate	1
1.2 Structure	2
1.3 Review of Recent Work and Experimental History	5
1.3.1 Ising-like behaviour and E_8 symmetry	14
1.3.2 Low Temperature Physics and Predictions	15
Chapter 2 Crystal Growth and Initial Characterization	17
2.1 Floating Zone Crystal Growth	17
2.1.1 Advantages of the Floating Zone Method	18
2.1.2 Disadvantages of the Floating Zone Method	19
2.1.3 Theory of the Floating Zone Method	19
2.2 X-Ray Diffraction	27
2.2.1 Diffraction Theory	27

2.2.2	Powder Diffraction	31
2.2.3	Laue Diffraction	32
2.3	Floating Zone Growth of CoNb_2O_6	33
2.3.1	Oxide and Ceramic Preparation	33
2.3.2	Pre-melt and Growth	38
2.4	SQUID Magnetometry	41
2.5	Sample Preparation	44
Chapter 3 Low Temperature Specific Heat Measurements of CoNb_2O_6		
	46	
3.1	Introduction to Specific Heat Measurements	46
3.2	Room Temperature to 2 Kelvin	49
3.3	Below 2 Kelvin	52
Chapter 4 Muon Spin Rotation Theory		57
4.1	Introduction to Muon Spin Rotation	57
4.1.1	Pion Production and Decay	57
4.1.2	Muon Production and Decay	59
4.1.3	Muon Spin Rotation and Relaxation as a Probe of Local Magnetism	65
4.2	Zero and Longitudinal Field μSR	66
4.2.1	Static Magnetism	68

4.2.2	Dynamic Magnetism	71
4.2.3	Overall Remarks	72
4.3	Transverse Field μ SR	73
Chapter 5 Muons Spin Rotation Measurements of Cobalt Niobate		76
5.1	Facilities	76
5.1.1	LAMPF Instrument	79
5.1.2	Dilution Refrigerator	79
5.2	Transverse Field μ SR Experiments	83
5.3	Longitudinal and Zero Field μ SR Experiments	85
Chapter 6 Conclusions		92

List of Figures

1.1	The Structure of Cobalt Niobate	4
1.2	Magnetic Octahedra in Cobalt Niobate	5
1.3	Magnetic Octahedral Chains in Cobalt Niobate	6
1.4	The Phase Diagram of Cobalt Niobate with H Parallel to the c-axis	12
1.5	Cartoon of the Intra- and Interchain Connections from Equation (1.1)	14
2.1	Image of a Frozen Zone in an Optical Floating Zone Furnace . . .	21
2.2	Schematic of an Optical Floating Zone Furnace	21
2.3	A Cartoon Depicting Bragg's Law	29
2.4	Pressed Rod of Cobalt Niobate	37
2.5	Result of a Pre-melt of Cobalt Niobate	39
2.6	A Cobalt Niobate Crystal Grown in the Optical Floating Zone . .	41
2.7	Magnetic Susceptibility of Cobalt Niobate Measured by SQUID Magnetometry	43
2.8	Cobalt Niobate Magnetic Susceptibility Measured by Hanawa . .	43
2.9	Magnetic Susceptibility of Cobalt Niobate up to 300 K at 100 Oe, Measured by SQUID Magnetometry	44
2.10	The Screw Dislocation During Growth	45
2.11	Prepared Slice for Specific Heat Measurements Before the Final Cut	45

3.1	Plot of Specific Heat versus Temperature with Inset	51
3.2	Plot of Specific Heat versus Field	52
3.3	Specific Heat Capacity and Relaxation Time Constant below 1 K	54
3.4	Low and High Temperature Specific Heat of Cobalt Niobate . . .	55
3.5	Alternative Heat Capacity Plot of Cobalt Niobate	56
4.1	Probability of Direction of Emission of the Positron upon Muon Decay	63
4.2	A Schematic of Muon Precession around the Internal Magnetic Field	68
5.1	The OMNI-LAMPF Instrument Fit with Gas Flow Cryostat . . .	80
5.2	The Oxford Dilution Refrigerator and Spectrometer	82
5.3	The Fourier Transform for Runs 5121 and 5126	84
5.4	Plot of Fit Values of ζ for Cobalt Niobate	88
5.5	Plot of the Muon Relaxation Rate for Cobalt Niobate	89
5.6	Cobalt Niobate Asymmetries at Zero Field with Varying Temperature	90
5.7	Cobalt Niobate Asymmetries at Constant Temperature with Vary- ing Longitudinal Field	90
5.8	Cobalt Niobate Asymmetries at Constant Longitudinal Field with Varying Temperature	91

List of Tables

1.1	Lattice Parameters of Cobalt Niobate	3
1.2	Wyckoff Positions of the Atoms in Cobalt Niobate	3
2.1	X-ray Wavelengths for Selected Anodes	31
2.2	Table of Reaction Products for Cobalt Niobate	35
4.1	Muon, Proton and Electron Properties	60

Chapter 1

Introduction and Theoretical Background

1.1 Cobalt Niobate

Cobalt niobate, CoNb_2O_6 , is a material that was initially crystallographically solved in 1979[1]. A recent resurgence in research on this material has begun after a theoretical connection between the mathematical E_8 symmetry group and the potential of this material to be a physical realization of that Lie algebra. The E_8 symmetry group is important because it represents the highest possible symmetry operator in nature that has been predicted so far by mathematics. Symmetry operators in Physics are particularly important because they generally describe critical phenomenon; for example, the $U(1)$ symmetry group is key in modelling the critical behaviours of time-reversal symmetry breaking and cooper pairing of electrons.

Recent work in neutron scattering has shown that this level of symmetry is a possible explanation, although it is not conclusive[2]. What is known is

that the phase diagram at low temperatures is extremely rich, with groups reporting paramagnetism, Néel ordering, incommensurate spin behaviour, ferrimagnetism as well as the following field and temperature induced states: low temperature, high field ferrimagnetism; high temperature, high field ferrimagnetism; and high field, high temperature ferrimagnetism mixed with high temperature incommensurate behaviour. The phase diagram can be seen in figure 1.4. This exotic behaviour and large number of magnetic transitions make CoNb_2O_6 an ideal candidate for investigation with muon spin rotation (μSR) and other techniques[3][4].

In addition to the phases listed above, theoretical calculations have been done that seem to indicate that this material exhibits quantum critical behaviour in the neighbourhood of 5.5 Tesla of magnetism applied along the b-axis[2].

To investigate this material, its magnetic properties and its phase space, the preparation and characterization of high quality cobalt niobate crystals was required. This thesis describes the work done to date on this system, gives the conclusions that can be drawn so far and attempts to chart a future direction for this work, given some still unsolved questions.

1.2 Structure

The atomic structure of cobalt niobate has been solved by several groups [1][5], and other than a translation of atomic co-ordinates within the unit cell there is agreement on the refinement. The structure itself is space group 60, P_{bcn} , which is an orthogonal, primitive space group with the properties of

mirrors in the b and c planes with a crystallographic n-glide. Cobalt niobate is part of a family known as 'Columbites', which are minerals of the form MNb_2O_6 where M are divalent metal atoms, such as $M=(Co, Mg, Fe, Mn, Ca, Cu, \text{etc.})$ [3].

The generally accepted lattice parameters were originally solved by Weitzell and are given in Table 1.1. From that table we find that $a \neq b \neq c$ and $\alpha = \beta = \gamma = 90^\circ$, which is the definition of an orthorhombic lattice. The Wyckoff positions are listed in Table 1.2 and put the Cobalt atom on a special position that generates a quadrupling of the atoms in the unit cell, while the niobium and oxygen atoms are on special positions that generate an octupling of the atoms in the unit cell. A drawing of the structure is shown in Figure 1.1.

A	14.1475 Å
B	5.7120 Å
C	5.0446 Å
α	90.0000°
β	90.0000°
γ	90.0000°

Table 1.1: Lattice Parameters of Cobalt Niobate[1]

Atom	Wyckoff Symbol	X-Coordinate	Y-Coordinate	Z-Coordinate
Co(1)	4c	0.0000	0.3182	0.2500
Nb(1)	8d	0.3384	0.3242	0.2555
O(1)	8d	0.0952	0.1034	0.0671
O(2)	8d	0.4247	0.1153	0.1116
O(3)	8d	0.2477	0.1238	0.4307

Table 1.2: Wyckoff Positions of the Atoms in Cobalt Niobate[1]

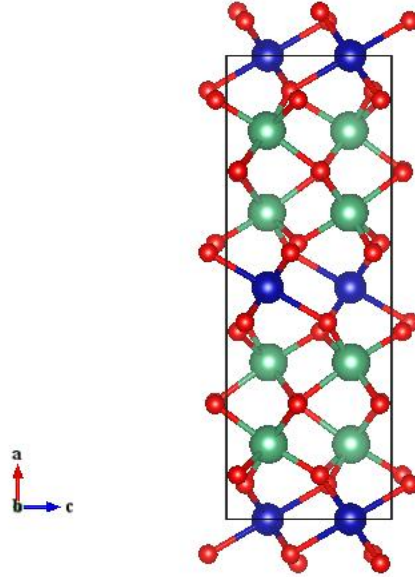


Figure 1.1: The Structure of Cobalt Niobate
(Blue = Co, Green = Nb, Red = O)

With respect to bonding, the cobalt atoms are in the Co^{2+} state, the niobium atoms are in the Nb^{5+} state and the oxygen atoms are in the O^{2-} state. This leaves the niobium and oxygen atoms in states with full electron shells, implying that they will not be magnetically dominant. The cobalt atoms, however, have an unpaired electron and will act like $\frac{1}{2}$ integer spin particles. This gives a magnetic space group of P_{222} , which has a higher level of symmetry than P_{bcn} . We can see that the oxygen atoms form octahedral shells around the cobalt atoms, as seen in Figure 1.2, which isolates them from each other and the remainder of the lattice and gives rise to some of the interesting properties observed in cobalt niobate. Observing the crystal structure either with cobalt atoms only, or, for clarity, cobalt atoms surrounded by oxygen octahedra it is easy to see the zig-zag chains of cobalt atoms in the a-c plane as in Figure 1.3. Calculations and measurements performed by Mitsuda give a

spin canting angle of 31 degrees, alternating between chains in the a-c plane, or along the b-axis[6]. This gives rise to a very strong J_1 , or nearest neighbour, interaction along the direction of the chains, and very weak J_2 , or next nearest neighbour, coupling which links the chains. This will be further elucidated in the following sections on Ising-like behaviour and expected low temperature behaviour.

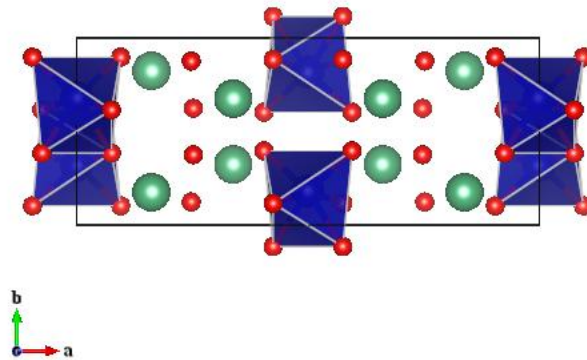


Figure 1.2: The cobalt niobate structure looking along the magnetic octahedral chains

1.3 Review of Recent Work and Experimental History

The first study of work that would be considered as part of the experimental history was published in 1977 by Maartense and Yaeger[7]. This group was the first to report magnetic data on cobalt niobate at low temperatures on a single crystal sample. At this point powder neutron diffraction had been performed

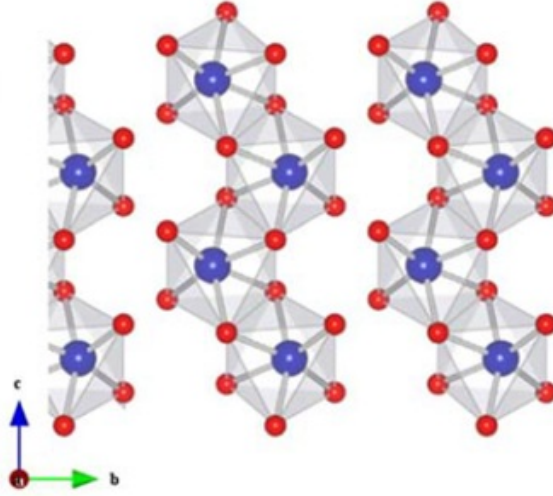


Figure 1.3: The cobalt niobate magnetic structure looking perpendicular to the octahedral magnetic chains

and had determined that there was spin collinearity along the a-axis. This was shown to be incorrect by future studies found below. The Maartense data was the first, at low temperature, to propose a spin-canted phase, where they reported a canting angle of 34 degrees. Additionally, because of the anisotropic measurements between the a and c directions they infer that the minimum size of the magnetic sublattice to properly characterize this material is at least a system of 4 spins. Additionally, they determine there is an intermediate state between the paramagnetic phase and the antiferromagnetic phase that changes with applied field.

A further study was performed in 1979 by Scharf et al.[8] to look at the magnetic susceptibility of cobalt niobate at low temperature. They were able to classify the magnetic space group as P_{222} and performed a study of magnetic susceptibility changes depending on crystallographic orientation. This showed that there was little to no dependence of magnetic susceptibility with field

applied along the b-axis, and from this and measurements along the a and c axes that the spins were canted in the a-c plane. At the temperature range between the two transitions in cobalt niobate, at 1.9 K and 2.9 K, neutron scattering was performed finding a peak at $(0 \frac{1}{2} 0)$ and satellite peaks at $(0 \frac{2}{5} 0)$ and $(3 \frac{3}{5} 0)$ corresponding to a screw axis at 59 degrees from the x-axis, or canted 31 degrees into the a-c plane.

In 1992, Hanawa et al.[9] looked at sintered powder samples of cobalt niobate with both AC and DC susceptometry and heat capacity measurements down to 1 K. They note that the region between the two transition temperatures at 1.9 K and 2.9 K is antiferromagnetic but that the antiferromagnetism seems to disappear below 1.9 K. The phase below was undetermined in this study, although they recommended neutron diffraction as an avenue for determining this. Hanawa et al. noted that the application of a magnetic field of 500 Oe restored the antiferromagnetic behaviour. In the heat capacity data there was a sharp drop at the upper transition and then a shoulder that died off at the lower transition. This is similar to what is seen in future work.

The 1994 follow-up work by Hanawa et al.[3] extended the previous work by examining the anisotropy of crystal orientation on the results of the specific heat capacity under applied magnetic field. Single crystals were grown via the flux method utilizing sodium borate, $\text{Na}_2\text{B}_4\text{O}_7$, as the flux material for growth. This investigation found phase transitions at 1.9 K and 2.9 K, which was in agreement with previous work. Measurements were made with the applied fields parallel to the a, b and c axis directions. The results showed that with field applied along the b-axis there was only a very small change of

susceptibility just above 2 K. Likely this was due to a sample misalignment, as previous work as well as the present work show that there is no change evident. A small misalignment of the crystal in field would show a change based on spins oriented in the a-c plane. Based on the alignment that we performed the misalignment would be more than one degree, but on the order of degrees. AC susceptibility changes were evident in the a and c alignments at 1.9 K and 2.9 K. The material was examined in changing fields, where the transition peak was shown to change from a strong peak to a smoothed curve with increasing field. Hanawa used their data, along with the Scharf and Maartense data to construct an updated magnetic phase diagram with changing field. Based on the hysteretic behaviour that Hanawa found, they proposed a six spin sublattice model would better described the system than the previous four spin model proposed to describe the previously identified spin-flip phases. Hanawa also found that there was a different downturn in the specific heat with applied field at temperatures between 0.5 K and 1 K.

In 1994, Mitsuda et al.[6] did further experiments on a flux grown crystal of cobalt niobate. They examined the region below 3 K with neutron scattering attempting to better understand the chains. They found that the system approximates a 1D Ising chain, or is a quasi-1D Ising chain, but is expected to have recognizable magnetic order in other dimensions. The examination of the b^* direction seemed to indicate that the chains themselves behave ferromagnetically, not antiferromagnetically. Additionally, Mitsuda found that as the temperature is decreased, peak intensity moves towards $(0 \frac{1}{2} 0)$ indicating that the helical spins are aligning antiferromagnetically. It is inferred that there is, at the lowest probed temperatures near the lower transition a

2D-like characteristic emerging, which indicates the importance of interchain coupling and its competition with the Co^{2+} single ion anisotropy. The single ion anisotropy comes from a splitting of the crystal field. Co^{2+} has an outer shell electron configuration of $3d^7$, which for iron-type elements is part of the outer electron shell. This shell will experience the inhomogeneous electric field produced by neighbouring ions. This effect changes the \mathbf{L} and \mathbf{S} vectors so that their states are no longer given by their J value, and the $2L + 1$ sublevels belonging to a given L that are nominally degenerate in the free ion are now able to be split. This means that the atom has a lower energy state in the configuration when the electron cloud is closest to the positive ions[10]. This coupling is hypothesized by Mitsuda et al. to be the reason why, at the lowest temperatures, the spin relaxation time starts increasing.

In 1995, Heid et al.[11] performed a series of neutron scattering experiments to better understand the spin flip phases discovered the year prior. Their work focused primarily on a magnetic field applied along the c -axis. It was determined that as field was increased at temperatures below the 1.9 K transition the propagation vector of the spin flip changed from $k_y = 0 \frac{1}{2} 0$ to $k_y = 0 \frac{1}{3} 0$ between 0.30 T and 0.36 T applied field before transitioning to the paramagnetic phase. This transition occurred strictly from the first spin flip phase to the paramagnetic phase in the temperature range between the two transitions. Heid et al. also used their measurements to determine that in the a - c plane the canting angle, γ , of the spins was 29.4 degrees in the a - c plane. Additionally, Heid et al. noted that there were long relaxation times at low temperature, and predicted that the heat capacity anomalies with applied field at low temperature were due to the system not being allowed to come to

equilibrium at the lowest temperatures. It was commented that the magnetic phase transition at low field and at 2.9 K actually initially had a slight increase in transition temperature with low field applied, and it was noted that this behaviour might be the result of an increase in the exchange interaction due to suppression of the magnetic fluctuations by the external field. This suppression is of note because although Heid et al. concluded that this system acts as a low-dimensional system, the Ising-like characteristics can be questioned due to a 2 percent increase in the Néel temperature stemming from single-ion anisotropy, in compared to what would be expected strictly by theory for a 1D system.

In 1997 Heid et al.[12] had a subsequent paper further increasing the density of the magnetic phase diagram due to further data collection. Heid et al. proposed an additional three spin flip phases in the c-axis direction, with two of those phases sharing common boundaries when the same fields were applied to the a-axis. This spin flip phase was discovered by applying a field 40 degrees to the c-axis, and was identified by its four-fold unit cell with propagation vectors $K_1 = (0 \frac{1}{4} 0)$ and $K_2 = (0 \frac{1}{2} 0)$. It was calculated that simple interchain interactions were not sufficient to explain all the features of the phase diagrams. At this point they calculated that the dipole-dipole interactions in the material were on the same order of magnitude as the interchain interactions, implying that they must be accounted for in the spin-flip regions.

In 1999 Kobayashi et al.[4] did an extensive survey of the phase space of cobalt niobate down to 0.2 K in fields up to 4.4 kOe with H parallel to the c-axis using neutron scattering. The results from this paper present a slightly

different picture than the results from Heid et al. in 1997, and further subdivide the phase space into different spin flip phases, comprised of ferrimagnetic ordering instead of ferromagnetic ordering. The incommensurate spin phase where there is spiral ordering was subdivided into high and low temperature orderings, and the ferrimagnetic phase has at least four different ordered states, or states with different magnetic propagation vectors, with varying field and temperature. It also shows some hysteretic behaviour. Kobayashi et al. recognize the extremely long ordering time, which they believed was responsible for the increased number of phases reported. From their conclusions, it is uncertain if they waited for the spins to enter the thermal ground state before they began measurements. Kobayashi et al. have provided the most comprehensive phase diagram for cobalt niobate so far, and the diagram with H applied parallel to the c -axis is given in figure 1.4.

In 2010 Coldea et al.[2] expanded on the work by Lee et al. from 2010 by further elucidating the concept of the quantum phase transition in cobalt niobate at a critical field of 5.5 T. Using neutron scattering, they showed that, at low temperatures, the application of a transverse field from 0 T to above 5.5 T this material transitions from a magnetically ordered state to a quantum paramagnet where the spins are represented by quasiparticles which oscillated between the two degenerate ground states along the $+z$ and $-z$ axes. Coldea et al. also connect their results to potential E_8 symmetry, the highest mathematically symmetric group that has been predicted to exist. In zero field below 40 mK gapped continuum scattering due to kink pairs were found to create a continuum of discrete bound states. Calculations were done to show that these results are consistent with modelling and that the lowest two

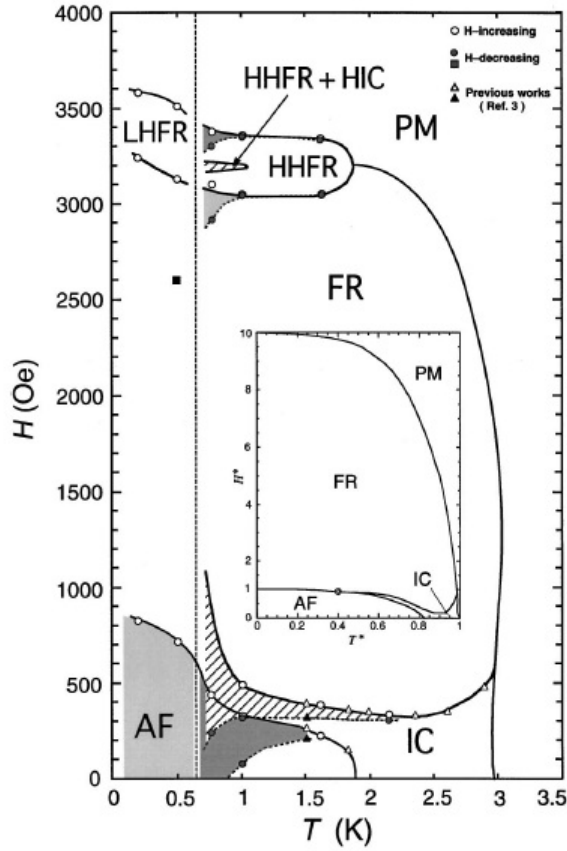


Figure 1.4: The Phase Diagram of Cobalt Niobate with H Parallel to the c -axis[4]

states are consistent with the lowest two of 8 states predicted mathematically by Zamolodchov[13] in 1989.

In 1989 Zamolodchikov[13] derived a conformal field theory for the Ising model where $T=T_c$. From this he was able to solve the Ising model in a non-zero magnetic field. His solution generated a series of 8 theoretical particles from the scattering matrix. The properties of these pseudoparticles have a peculiar form, in that the masses of each represented poles in the complex plane. These masses end up being the exponents of the Lie algebra E_8 , which

is the Lie algebra with the largest number of symmetry operators that has been derived to date. This makes Coldea et al.'s assertion that cobalt niobate is a candidate for E_8 symmetry in nature an important fact, as symmetry breaking in a material is the chief way in which we get phase changes.

Lee et al.[14] furthered the study of the quantum criticality and the Ising-like nature of cobalt niobate in a theory paper published in 2010. Lee et al. constructed a model with nearest neighbour interactions along the chains in the direction of the c -axis, J_0 , as well as next nearest J_1 and J_2 interactions in the Hamiltonian, (1.1)[14] along the triangular cobalt sublattice. Lee considers J_0 to be the strong interchain interaction, while J_1 and J_2 are the two interchain distances arranged in an isosceles manner, as shown in figure 1.5. From this they were able to extract a model where a parameter α was used as a measure of deviation of the triangular lattice from an equilateral to isosceles case, where we find α is a slight deviation from 1 in the cobalt niobate case. From this model antiferromagnetic, incommensurate and two Néel ordered phases were predicted, as well as the quantum critical point. This was done for values of α equal to 1, 0.99 and 0.9 as a function of applied perpendicular field, h_\perp .

$$\begin{aligned}
 H = J_0 \sum S_{z;\mathbf{r}^z} S_{z+1;\mathbf{r}^z} + J_1 \sum S_{z;\mathbf{r}^z} S_{z;\mathbf{r}+\mathbf{a}_1^z} + J_2 \sum S_{z;\mathbf{r}^z} S_{z;\mathbf{r}+\mathbf{a}_2^z} \\
 + J_2 \sum S_{z;\mathbf{r}^z} S_{z;\mathbf{r}+\mathbf{a}_3^z} - h_\perp \sum S_{z;\mathbf{r}^x}
 \end{aligned}
 \tag{1.1}$$

In 2011 Sarvezuk[5] et al. further explored this material with both heat capacity and neutron diffraction. They confirmed previous results, but also observed additional transitions in the material. First, another magnetic phase

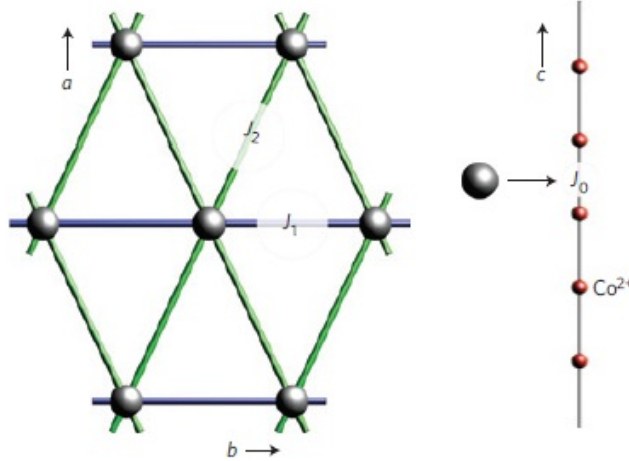


Figure 1.5: Cartoon of the Intra- and Interchain Connections from Equation (1.1) from [14]

transition was found at 2.5 K with a propagation vector of $(0 \ 0.4 \ 0)$. Second, at 1.4 K more measurements were taken and it was determined that there are two co-existent phases, one with the propagation vector $(0 \ \frac{1}{2} \ 0)$ and one with a propagation vector $(\frac{1}{2} \ \frac{1}{2} \ 0)$, indicating that a further analysis of this material, focusing on the effects of inter- and intrachain coupling is needed to better understand the low temperature behaviour of this material.

1.3.1 Ising-like behaviour and E_8 symmetry

From both the theory and the experiments reviewed above, we see that this material acts in an Ising-like manner, and that the niobium atoms act, magnetically, an order of magnitude more weakly than the interactions between the cobalt atoms. The oxygen atoms cage the magnetic cobalt atoms in linear chains. The material exhibits magnetically easy axes along these linear chains at an angle of 31 degrees from the a-axis in the a-c plane. The description of

this system is only quasi-1D, however, as evidence of 3D ordering is seen in some cases, as referenced above. However, the system can be, and has been, well characterized using the 1D-Ising model.

The methods we employ for study of this material will not be able to probe whether or not there is E_8 symmetry. The fact that this material could be a member of this Lie algebra class is of interest because symmetry breaking is the prime way that we see a change of the state of matter in materials. A material that falls in this class would theoretically have the potential for a very rich phase diagram, as well as the potential for novel phases. These phases would likely be expressed most readily as changes at the lowest temperatures, which is the area that is probed in this thesis.

1.3.2 Low Temperature Physics and Predictions

At present, from the literature review above, there is some lack of definition on the phases that are currently being expressed in the material at low temperatures. A phase boundary at 1.9 K and at 2.9 K at 0 T is well defined, although other states are proposed and have been classified in several ways. Of importance is the fact that, at the lowest temperatures, all phases are defined as antiferromagnetic at the lowest fields, passing through a ferromagnetic regime and into a paramagnetic phase with increasing temperature. Some papers have referred to a very long spin relaxation time, although it was never expressed explicitly whether or not the spins were allowed to completely thermally relax before making a measurement and no complete study on the relaxation time constant at temperatures below 1 K has been completed. This

thesis will look at these areas to determine if we yet have a complete picture, and what steps will be necessary to better determine the ground state of cobalt niobate.

Chapter 2

Crystal Growth and Initial Characterization

In this chapter I describe the techniques used to grow and characterize the crystal sample of CoNb_2O_6 , including optical floating zone growth, x-ray characterization and diffraction, and SQUID magnetometry. Additionally, information regarding the specifics of the growth and characterization results will be elucidated.

2.1 Floating Zone Crystal Growth

Optical floating zone crystal growth is one of the most ideal techniques available for the creation of high-purity, single crystalline structures composed initially of chemical oxides. The primary commercial limitation of this system is that the diameter and length of the crystals that can be grown in this system are restricted by the technique, in contrast to more commercialized methods, such as Czochralski pull. This means that growth by the floating

zone is primarily for research purposes, although there are some exceptions for specific applications.

2.1.1 Advantages of the Floating Zone Method

The primary advantage of the optical floating zone method is that no crucible is necessary, which removes a significant source of contamination from the system. Additionally, a steady state condition can be obtained in the melt phase of the material. By this it is meant that the volume of material that is molten at any given time is essentially constant when the growth parameters have stabilized. The steady state condition also allows for controlled, uniform doping of a material by an off-stoichiometric inclusion of an excess amount of a particular oxide. Further, both congruently melting materials and incongruently melting materials, or materials where the oxide components decompose when melted, can be grown. The latter is done by the travelling solvent method, where a solvent, or flux, either as a third compound or one of the oxides in the case of self-flux, is used to keep the material in a peritectic state, where a liquid and a solid react to form a output solid[15]. The flux method of crystal growth, which has been performed by other groups on cobalt niobate, uses a similar technique, although since it is crucible-based the output crystals would typically be smaller and with higher levels of impurities. A chemical analogy for flux growth can be drawn between the materials and the concept of a chemical catalyst, where the difference is that the reaction is not being sped up, but rather facilitated by the solvent material. Cobalt niobate was prepared from cobalt oxide and niobium oxide. Both of these oxides are

congruently melting materials so no other flux was required for this particular growth. For self-flux and flux growths, the lack of incorporation of the solvent into the material in any appreciable amount occurs for the same reason that high purity crystals are obtained from this method. This effect is described in a future section of this chapter.

2.1.2 Disadvantages of the Floating Zone Method

The disadvantages of this method include the fact that materials with high vapour pressures are unsuitable for growth, as they will evaporate or sublime rather than forming or staying in the melt. Materials that are highly viscous or have low surface tension are also unsuitable, or far more difficult to grow, because the effects of thermal fluctuations in the system make it difficult to maintain or find stable growth conditions without causing zone collapse[15]. Finally, materials that go through phase transitions when cooling are also unsuitable, as the crystal will in the best case, crack, and in the worst case disintegrate due to the stress on the lattice during the phase transition due to the rigid shape of the crystal.

2.1.3 Theory of the Floating Zone Method

An image of the interior of an Optical Floating Zone furnace with a seed and feed rod that have a zone intentionally solidified is given in Figure 2.1 and a schematic representation is given in Figure 2.2. The optical floating zone technique uses an optical furnace as well as specially prepared ceramic oxide

rods. The furnace itself generally consists of either two or four ellipsoidally shaped mirrors arranged so that they have a common focus point. The foci of the ellipsoids that are not common between mirrors will have a high-powered light bulb designed primarily to be a high-flux infrared source. The light bulbs are generally halogen bulbs, although the new, highest temperature furnaces now contain xenon-based lamps. At McMaster, the bulbs presently used allow for a temperature of up to approximately 2,300 degrees Celsius to be obtained at the centre of the zone. During the growth, the power output of the lamps are used to measure 'temperature' in a coarse way. A calibration curve exists based on the melting point of numerous materials, but the melting point is influenced by size, shape and quality of the material so there is no exact method used to determine temperature. As the bulbs wear, their ability to covert input power to output infrared radiation decreases, so even using power computed through input voltage and current is inexact. Further, the diffuse nature of the infrared radiation supplied to heat the ceramic must be considered.

The light bulbs themselves comes in varying wattage: 500 W, 1 kW and 1.5 kW. Higher output wattages allow for higher temperatures to be obtained. The trade-off, however, is that the focus of the bulb is far more diffuse, owing to the larger filament required for the higher power, resulting in less concentrated energy deposition in the zone.

The primary purpose of the lamps is to supply thermal energy to the system. The light bulbs used are essentially the same as any household light bulb, which is to imply that they operate by passing a current through a highly resistive wire, which in turn creates a significant amount of thermal

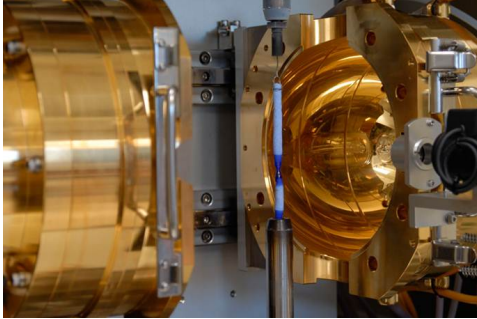


Figure 2.1: Image of a Frozen Zone in an Optical Floating Zone Furnace

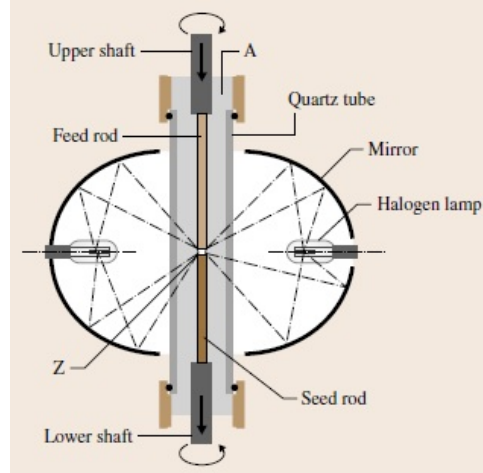


Figure 2.2: Schematic of an Optical Floating Zone Furnace. A = Atmosphere, Z = Floating Zone[15]

energy through infrared radiation emission processes. The energy is focused onto a stoichiometrically prepared ceramic rod located slightly above a seed crystal or ceramic. The rod itself is rotated to provide a uniform energy deposition over the rods surface, as it cannot be guaranteed that the filaments are uniform or that there are no non-uniform aberrations with respect to the mirrors. Additionally, with multiple bulbs the output wattage is dependant on the filament, which is measurably different due to both manufacture and wear. During the growth there is an offset voltage that can be applied to increase or decrease one lamp independently, allowing the crystal grower to tune the light bulbs to equal output powers.

It should be noted that the thermal gradient mentioned prior extends not solely vertically, but also radially into the centre of the melt. This is simply because the surface of the crystal is being heated by incident radiation, while the centre of the melt is heated through liquid radiative transfer. The effect of

this is that the crystal will begin to form in the radial centre of the melt, generally hidden from view. Occasionally, with materials that grow preferentially in odd planes, for example in the (102) crystallographic direction, the zone will be distorted to one side as the crystal tries to 'poke' through the liquid layer in the direction of anisotropic growth. An explanation of directional notation is briefly provided in the section on diffraction later in this chapter.

The seed rod is located below the zone and provides a clean surface for the new crystal to be grown on. Preferably, the seed is an oriented single crystal of the desired material, which provides for an ideal structure to start growing upon. If you consider the growth on the atomic level as equivalent to the stacking of balls in a lattice arrangement, obviously starting with a perfect stack and growing on top of that structure gives the most ideal start to the growth, or at least the one likely to have the least number of problems. If a single crystal of the desired material is not available, either a crystal of similar space group with relatively close lattice parameters or a pressed pre-reacted powder of the same material is the next choice for use. As an example of the first case, growing one member of the rare earth titanate family using the seed of another rare earth titanate has been done at McMaster for the reason that the space groups are identical and the lattice parameters are nearly so. The shear bulk of the second material in the melt will take over the lattice.

The feed rod is hung from a hook using platinum or nickel wire, depending on the reactivity of the oxides being used in the growth and their reaction chemistry, while the seed rod or seed crystal will be wire mounted, again using platinum or nickel wire, into a ceramic holder attached to a base that screws

into the lower half of the floating zone system. With a pressed pre-reacted powder being used, one consideration is that the density of the pressed rod is likely at least thirty percent lower than the final expected density of the crystal, which implies that there are large spaces in the ceramic. Upon initial melt the material will first seep up into these voids in the ceramic due to surface tension before the liquid melt can be used to start to form a crystal.

Thermal power in the floating zone is raised until the melting point of the material by increasing the voltage and current supplied to the lamps. Generally, at this point, the temperature is either sustained or, in the case of less viscous materials, decreased, since viscosity is a function of temperature and slightly lower temperatures can therefore be advantageous. This is possible to do without freezing the zone since melting is a first order phase transition and the latent heat of the system plays an important role in the stability. The ideal temperature for the growth is that which allows for maximum thermal input without creating a melt that has a viscosity so low that the liquid in the floating zone will spill or drip.

The rod, seed and floating zone are contained within a sealed quartz tube. This is done so that the growth atmosphere can be controlled. It is not uncommon to use air for materials that aren't expected to react with the trace gases, or that are likely to form the desired state regardless. However, for materials with several possible phases or allotropes it is often desirable to create one of the following: oxidizing conditions, by using oxygen gas; slightly reducing conditions, by using something inert like argon gas; or, potentially highly reducing conditions, with a mixture of carbon monoxide and carbon dioxide

being an example of a reducing agent recently used in the crystal growth lab to try and form different valencies of vanadium to create different types of lutitium vanadate[15][16].

In the initial stages of growth, even sometimes when starting with a single crystal seed, the material created will have polycrystalline, randomly oriented domains. This is a function of the connection of the liquid zone, as it is a very sudden, extreme process. Initially the tip of the feed rod is made molten and then lowered to the seed and put into contact. This creates a significant ‘shock’ cooling and will form the first grains. Using a single crystal simply gives a preferred direction and increases the likelihood that the initial grains are somewhat aligned. The radial extent of the crystal is determined by the width of the seed rod, the amount of material and the surface tension. As the crystal grows, a few co-aligned grains, or hopefully one single grain will become dominant and force other grains to the edge of the crystal where they will be overrun completely. As grains compete the surfaces of competing grains have a high amount of entropy due to lattice mismatch. When one grain, or several co-aligned grains push the other grains to the edge of the crystal, they can no longer grow and will terminate. As this happens, power needs to be monitored and the temperature potentially lowered due to the decreased entropy at the surface of crystal formation. Otherwise it is the same as increasing the temperature of the melt which can lead to instability due to decreased viscosity with temperature increase. Generally, it is assumed that materials will require up to 2 centimetres of growth to push out enough grains that the grower can be confident that the crystal will be a single crystal instead of a polycrystal.

The lower limit, which some highly stable materials can achieve for transition from this polycrystalline phase, would be the approximate diameter of the rod.

Once the floating zone is established counter-rotation of the seed and feed rods is performed to allow for convective mixing of the melt. Additionally, if there is misalignment of the seed and feed rods the counter rotation will show this. However, once the growth is established the growth direction will be preferentially along the combined axis of the system and the surface tension of the zone will help to hold the centre of the zone relatively fixed.

Within the melt, it is important to know that as the growth stabilizes, any impurities in the melt will tend to remain within the melt itself, as opposed to forming a portion of the crystal lattice as a defect. The primary reason for this is an entropically based argument. The atoms are very slowly competing to form layers, and the most entropically favourable particle to fill a particular position on the lattice is the one that belongs. Ergo, it is unlikely that an oxygen atom would attempt to fill the cation site, as an example. Any impurities in the original material that were not removed would be the wrong size, shape and/or charge to fill the vacancy in the lattice, especially when the vast majority of particles available in the melt are ideal for filling a vacancy in the crystalline lattice, so they too should remain in the melt.

Once the growth is stable, in the ideal case no further adjustments are made to thermal power, growth rate or rotation rate until the desired end point of the crystal growth is reached. This end point is determined either based on the size of crystal that can be grown in the machine or when the material prepared for the growth has been exhausted. Generally, the feed rate

of the feed rod is higher than the growth rate of the crystal due to packing density. A properly prepared rod will generally have a density of between 60 and 70 percent of the final material, which means a higher feed rate for the same diameter of a crystal as the rod. The biggest complications that arise once in the single crystal phase of growth are based on non-uniformity of the rod. Rods are all manufactured by hand, as described in the section on oxide and ceramic preparation, which means that even taking care, it is subject to non-uniform density and especially to non-uniform diameter, both of which will easily upset the balance in the zone. Instability can cause the liquid zone to drip down the crystal or can cause the zone to collapse quite suddenly. This is why when performing this method of crystal growth, especially for fast growth rates, continual monitoring is required.

A growth is ended by stopping motion in the zones and cooling the liquid zone until it becomes solid. This can be done at a rate where it solidifies completely and stays separate only due to the rotational motion, although typically as the zone narrows to between 1 and 2 mm diameter the decision is made to pull the zone apart by raising the feed rod. The resultant crystal is then allowed to cool in the growth atmosphere, generally with a cooling rate of the lamps between 3 and 5 percent power per hour. The reason for this slow cooling rate is to attempt to mitigate a thermal shock and quench of the crystal. Typically, if this is not done, cracking can occur in the crystal, degrading its overall quality. This is especially true if grain boundaries exist.

2.2 X-Ray Diffraction

Both powder and Laue x-ray diffraction were performed at several stages during the preparation, growth and characterization of this material. For materials that have not been previously grown locally, the importance of the characterization throughout cannot be understated if high quality materials for research are the desired output[17]. Diffraction theory provided in this section will focus mainly on Debye-Scherrer scattering, used for powder samples, and polychromatic beams used in Laue scattering.

2.2.1 Diffraction Theory

Interatomic distances within solid materials are typically on the order of Angstroms. The requirement to probe materials on this scale is that the wavelength of incident radiation must be below that of this average size. Using electromagnetic waves, wavelengths on this order fall into the x-ray band, and the respective minimum energy can be computed using equation (2.1) to be on the order of tens of keV[18]. Additionally, diffraction on this scale can be accomplished using beams of electrons and neutrons by treating them as waves using wave-particle duality[19]. However, these methods were used and therefore will not be described further.

$$h\omega = \frac{hc}{\lambda} \approx \frac{hc}{10^{-8}cm} \approx 12.3 \times 10^3 eV \quad (2.1)$$

Bragg found that crystalline materials formed patterns of intense peaks of diffraction under x-ray illumination that were not present in liquid sam-

ples. He attributed this to regularly spaced atoms located in repeating lattice planes a distance d from each other. He showed that the peaks were due to specular reflection from the atomic positions and that for peaks to be observed these reflections must interfere constructively. This is summed up by Bragg's law (2.2), where n is an integer number of wavelengths, λ is the wavelength and θ represents the angle of incidence, also known as the Bragg angle in this case. Because specular reflection is assumed, typically angles expressed in crystallography are twice the Bragg angle, and are called 2θ angles.

$$n\lambda = 2d\sin\theta \quad (2.2)$$

Diffraction is expected at multiple angles, since as the incident beam is rotated different atoms in different planes will constructively interfere with each other. The distances that are measured using Bragg's law are being measured in Fourier space, or phase space since they are interplanar distances. Each set of planes can therefore constructively interfere. The way this is indexed is called Miller notation, and is expressed as the co-ordinates $\{hkl\}$, which are the reciprocals of the plane corresponding to the vector direction, (xyz) , in the direct, or real, lattice space. To get the actual lattice parameters using the interplanar distances for an orthorhombic cell, which is the case for cobalt niobate, equation (2.3), the generic equation relating real and Fourier space, can be used. Additionally, it can now be easily seen that multiple reflections from multiple Miller planes will be found at corresponding angles for a single wavelength, generalizing Bragg's law as seen in equation (2.4) and is shown schematically in figure 2.3.

$$d_{hkl} = \frac{1}{\sqrt{\frac{h^2}{a^2} + \frac{k^2}{b^2} + \frac{l^2}{c^2}}} \quad (2.3)$$

$$\sin \theta_{hkl} = \frac{\lambda}{2d_{hkl}} \quad (2.4)$$

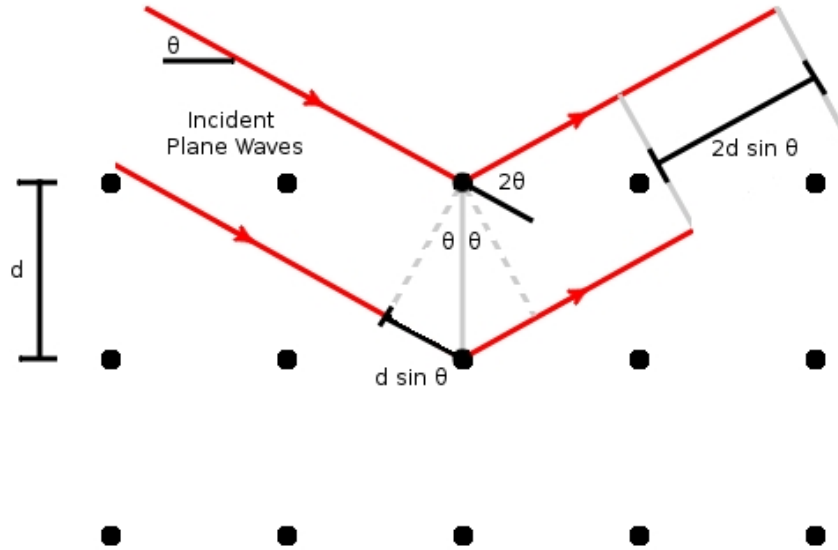


Figure 2.3: A Cartoon Depicting Bragg's Law[20]

In a laboratory setup, x-rays are generated when a beam of electrons is accelerated and strike a metal target, which for small molecules is commonly copper or molybdenum, although tungsten, cobalt, chromium, iron and silver are all used and have specific applications. As exemplified above, certain wavelengths of x-rays may interact with a sample in undesirable ways so alternate sources may be required. When x-rays are incident on a metal, they

are decelerated by interactions with the atoms in the lattice. A decelerating charge automatically produces electromagnetic radiation as a byproduct, and in the case of x-ray sources this is known as bremsstrahlung or braking radiation. Because the deceleration is particle dependant, a broad, continuous line shape is produced. The second generating mechanism of x-rays occurs when an incident electron knocks an electron from one of the inner shells of an atom. This in turn causes an electron from an outer shell to drop to the inner shell to replace it, which causes a corresponding emission of an x-ray photon. These are very sharp peaks corresponding to a quantified energy, and each peak is labelled by the atomic shell that the electron drops to, as well as by a Greek letter denoting the number of shells it dropped. For example, an electron from the L shell that is replacing a vacancy in the K shell would emit a photon at a wavelength labelled K_α . Correspondingly, a drop from the M shell to the K shell would be a K_β emission, while from the M to the L shell would be L_α . Due to the energy dependence on angular momentum, there are two transitions due to the splitting of energy levels for each wavelength, with the more intense, shorter wavelength being denoted with a further subscript 1, and the second with the subscript 2. Using a monochromator, a single wavelength, generally the K_α wavelength, can be extracted so that we have a known value of λ . For most applications it is acceptable to average the K_α photons, but should a higher precision be desired a curved monochromator crystal can be used to separate $K_{\alpha 1}$ from $K_{\alpha 2}$ [21]. Sample values for X-Ray wavelengths generated in this way are given in table 2.1.

Element	$K_{\alpha 1}$	$K_{\alpha 2}$	Mean K_{α}	$K_{\beta 1}$
Co	1.78892 Å	1.79278 Å	1.79021 Å	1.62075 Å
Cu	1.54051 Å	1.54433 Å	1.54178 Å	1.39217 Å
Mo	0.70926 Å	0.71354 Å	0.71069 Å	0.63225 Å

Table 2.1: X-ray Wavelengths for Selected Anode Materials[19]

2.2.2 Powder Diffraction

Powder diffraction is accomplished using the Debye-Scherrer method. The Debye-Scherrer method uses a monochromatic x-ray beam and polycrystalline, randomly oriented sample. The x-ray beam is mounted at the Bragg angle, θ , and an electronic counter is located in a mirrored position, so the total diffraction angle becomes 2θ . The arms holding the source and detector are then used to scan various angles in small steps, while recording the relative intensities. If all of real space was mapped, each reciprocal vector that scatters would be represented by a circular band of intensity centred around the sample at $2\theta = 0$ degrees, as well as at the antipodal point $2\theta = 180$ degrees.

Powder x-ray diffraction in this thesis is performed primarily by use of a PANalytical X'Pert Powder Diffractometer. The sample to be tested is generally either a powder or a crushed single crystal. The powder or crushed crystal is generally mixed with a small quantity of silicon powder. This is done so that there is a standard to compare the powder pattern to, as silicon has only a few very sharp, very strong peaks when diffracted. This allows for the 2θ values to be corrected for instrument error. The powder mixture is placed on a pure, single crystal silicon wafer as a background and as adhered using a mixture of petroleum jelly dissolved in toluene. The toluene is there as a solvent which evaporates off, forming a very weak 'glue' that holds the powder in place. This

powder is essentially at random orientations. This particular instrument can be fit with either a copper or cobalt source, with the copper being standard for small molecule diffraction. Cobalt is used when fluorescence, such as from an iron molecule, may present a problem. The beam setting typically used is a voltage of 35 kV and a typical powder diffraction scan spans the range of 20 degrees to 75 degrees in 2θ . The mounted powder is placed on a spinning platform. The rotation of this platform further randomizes the orientation in the beam, in case grains in the powder are preferentially aligned.

The results of the powder diffraction are converted and displayed using the DiffracPlus EVA software program provided by Bruker, which visualizes the spectrum and, through an extensive database that allows for additions from the ICSD repository of crystal structures, allows us to select the patterns we expect to see. In the case of an unidentified substance, we can attempt to perform peak searches through the internal database. In the case of the cobalt niobate, this was done on the cobalt and niobium oxides and we showed that the material the growth was started with was the pure and correct starting material. Additionally, powder samples analyzed before being pressed into rods showed that there was some pre-reaction, and that the level of pre-reaction increased with longer times and higher temperatures. This is described in the oxide and ceramic preparation section.

2.2.3 Laue Diffraction

Laue diffraction is performed using a polychromatic beam, so that multiple Bragg peaks are visible at the same time. Using an electronic area detector,

multiple points can be seen at a given time. This method is only useful for single, or nearly single crystals. Otherwise there will be far too many points to resolve, and we will see a ring similar to what would be expected in Debye-Scherrer scattering. Additionally, this method is not useful for determining values of lattice spacings for unknown materials, since the value of λ for a particular Bragg peak will not be known. The value of this technique is that a significant part of reciprocal space can be seen and projected onto a map, specifically in real time with our instrument. Multiple points can be used to determine the orientation of a single crystal, which was the use of this technique with respect to the cobalt niobate crystal.

2.3 Floating Zone Growth of CoNb_2O_6

This section describes the steps of a typical floating zone growth, and also contains specific information pertaining to the growth of the cobalt niobate crystal as appropriate. There does exist significant variability of preparation methods and procedures required for certain materials and these are briefly mentioned for completeness, but unless specifically stated were not performed for the growth of cobalt niobate.

2.3.1 Oxide and Ceramic Preparation

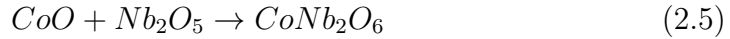
The first step in preparation for crystal growth is to create stoichiometric ceramic rods of the required materials. This is done by taking the oxides required, which for the purpose of this thesis were cobalt oxide and niobium

oxide, and separately sintering them at 300 to 400 degrees Celsius for 12 hours. The furnace is generally ramped at 100 degrees Celsius per hour and for these materials an air atmosphere was acceptable for sintering. This sintering is initially done for the purpose of drying out the oxides. Neither of the materials used are particularly hygroscopic, but some small mass loss was noted, indicating that some water was present in the samples. The cobalt and niobium oxides were sintered at 300 degrees for 12 hours.

Each of the powders was then x-rayed using powder x-ray diffraction to ensure that the correct material was present, as well as to check for any other major impurities in the system. Although we try to use the highest purity materials available, especially when using rare earths it is very difficult for providers to create completely pure materials due to the difficulty in separating rare earth oxides from each other. However, from the previous section on the theory of the floating zone method, a small level of impurity is easily tolerable.

The sintered oxides were then stoichiometrically mixed in a ratio that will create the final product, in this case cobalt niobate. The chemical reaction for cobalt niobate is listed in Equation (2.5) and its computed masses are given in Table 2.2. These powders are then ground, by hand, using an agate mortar and pestle which have been cleaned by an acid, until the mixture appears to be homogeneous. In the case of cobalt oxide and niobium oxide, the colours of the two materials were such that it was easy to tell when this had occurred. In the case of this material it was ground by hand for four hours. When the grinding was complete the materials were loaded into a alumina crucible. Generally crucibles are only used for a single material, or potentially a family

of doped materials. The single use nature, although increasing the cost of the method, ensures that contamination is minimized. Alumina crucibles, unlike the agate mortar and pestle, cannot be cleaned using an acid as that would etch the crucible, opening pores for contaminants or impurities to remain.



CoO	14.66 g
Nb ₂ O ₅	52.00 g
CoNb ₂ O ₆	66.66 g

Table 2.2: Table of Reaction Products for Cobalt Niobate

The combined oxides are then taken to a furnace for a ceramic pre-reaction. The materials are heated in the furnace so that they start to form the desired compound, although the heat is not so great as to make the mixture molten. At this stage particular gases may be used in a tube furnace to create oxidizing or reducing conditions if valency control is important. For the creation of cobalt niobate this was not an important factor due to its constituents preferred valency, its final valency and the congruent nature of the oxides and the chemical reaction. The heating and cooling profiles are generally similar to the sintering stage, although the temperatures are typically several times higher. In the case of the cobalt niobate, a temperature of 1100 degrees Celsius was used and the materials were pre-reacted for 24 hours in an air atmosphere.

When the cooled material is removed from the furnace, it will normally have changed from a powder to a hard ceramic. This ceramic will then be put into a bottle with zirconia pellets. This is then ball milled to regrind the

ceramic into a powder. The normal sequence is five minutes of grinding at 300 RPM followed by a cool-down of fifteen minutes, repeated three times. At this point the material is examined and a powder x-ray diffraction is performed to determine how much original oxide remains, and how much material has been pre-reacted and is in the correct phase, where appropriate. Should an insufficient amount not have been pre-reacted, the material will then be re-fired in the furnace, either using the same profile or one with a slightly higher temperature.

The ground powder can then be formed into a rod. Typically, this is done using a latex balloon as a form. The balloon is cleaned with alcohol and inverted to remove any powders or residue from the manufacturing process, as well as to check for any leaks or breaks in the latex. The rod material is then funnelled in slowly, compacted by hand and rolled until the desired length is created. At this point the air is pumped from the balloon, which is tied off. The balloon is then placed in a hydrostatic press, typically at a minimum pressure of 60 MPa for 15 to 20 minutes to help compact the material. After the hydrostatic pressing the balloon is cut off of the compressed rod using surgical scissors. This rod is then placed in an alumina crucible and annealed in the furnace, generally using the same profile and conditions as for the powder. This has the effect of further pre-reacting the material, increasing rod density and increasing rigidity so that the ceramic becomes increasingly unlikely to break. The first rod of cobalt niobate created was annealed using the same 1100 degree temperature for 12 hours. Upon removal it was found to have cracked. Future rods were annealed at 1250 degrees Celsius for 12 hours, aiming to pre-react further and increase the density to mitigate future cracking

while cooling. This was successful. Future pre-reactions of the powder were done with this higher temperature profile as well. A sample of a pressed rod is shown in Figure 2.4.

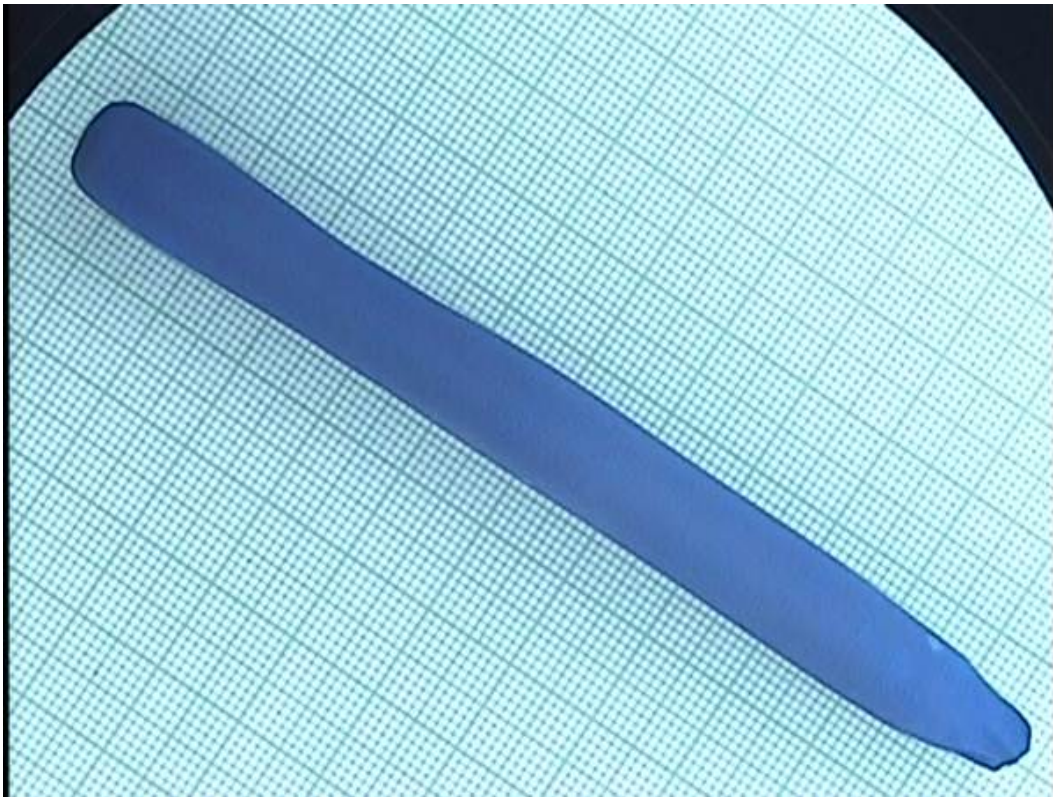


Figure 2.4: Pressed Rod of Cobalt Niobate

When the rod comes out of the furnace it is weighed to determine any additional mass loss and is measured to determine the approximate volume and density for comparison to the final material. This is useful in determining the ratio of feed rate and growth rate of the crystal. The ceramic is then prepared for mounting. Typically, the tapered end of the balloon is used as the base of the material, while the pointed end, from where the knot was tied, is the point of mounting. A channel can be cut with a scalpel to hold the

platinum or nickel wire to the feed rod, although this step is optional. The base can then be prepared by mounting a seed rod or crystal in the appropriate holder for the system and wiring it into position. The seed rod and the feed rod can then be mounted in the furnace and sealed in the quartz tube.

2.3.2 Pre-melt and Growth

The first attempt at a growth was done in the four mirror Crystal Systems optical furnace. The initial growth rate was set to 5 mm/hr, which was higher than the literature value but decided upon to allow us to quickly observe the initial characteristics of the growth. Almost immediately it was determined that the crystal was not going to grow this quickly and the decision was made to change the growth into a material pre-melt at 20 mm/hr. The pre-melt is a rapid liquification and solidification with the sole aim of increasing rod density and further pre-reacting the oxides. This is a step that is not generally necessary with most oxides, although making a rapid polycrystal to grow from can make a significant difference in the ease of the final growth since the density of the rod is almost that of the final product after a pre-melt. At the conclusion of a pre-melt, the seed and feed rods tend to be swapped so that material is not wasted. During the pre-melt, the external surface of the pseudo-boule appeared to have a unique, spiral-like structure. Subsequent Laue diffraction of the material showed an overlaid four-fold pattern, with the second layer offset by a few degrees rotation which seems to confirm that the lattice structure itself was spiralling during the pre-melt while attempting to form a crystal. The spiral had a pitch of approximately one to two millimetres. This carried

through into one facet of the final growths of the cobalt niobate crystals as well. An example of this effect can be seen in Figure 2.10. This effect has been observed in other niobates, such as barium strontium niobate[22].



Figure 2.5: Result of a Pre-melt of Cobalt Niobate

Two successful growths were done on pre-melted rods. In both cases, oxygen gas was selected as the atmosphere to be used. The system was purged with flowing oxygen for 20 minutes prior to sealing off the system. This is done in an attempt to limit all other atmospheric gases to trace amounts. For the first growth the pressure level was increased an additional 50 percent to approximately 1.5 atmospheres of pressure. The second growth was pressurized in a similar manner, although its pressure was increased to 1.6 atmospheres of pressure once the gas was heated, and so some gas was bled off to allow for conditions that were closer to the first growth. The increase in pressure with heating is expected from the temperature-pressure relationship of the ideal gas law, and it has become standard procedure to monitor and vent excess gas to ensure as repeatable conditions. This stems from a recent investigation into pressure and its affect on growth and growth stability in the floating zone[23]. Due to the stability of the material, the upper rotation rate of the feed rod was limited to 5 RPM, while the lower rotation rate of the seed rod was at the standard 30 RPM.

When the first crystal was grown the greatest difficulty was the fact that the diameter of the pre-melt varied significantly over the length of the crystal, showing a deviation of up to 25 percent from average. The melt began at approximately 87 percent power of the system, and was increased to 91 percent due to grinding of the seed and feed rods in the centre of the zone upon initial contact. The power was backed down over a number of hours until an approximately steady state was reached around 89.4 percent power. The rod was grown through the entire pre-melt and an effort to continue growth into the original ceramic material that was not pre-melted was commenced. This change required an increase in power. The growth exhibited less stable properties in the ceramic state, such as the formation of 'pebble-like' structures indicating that the power was slightly too low. Steady state conditions were eventually met, and allowed for a continued growth for several hours beyond the point at which the pre-melt was exhausted. The backfeeding rate, or growth rate, of the crystal varied from 0.5 mm/hr up to 2.1 mm/hr depending on the portion of the crystal being grown. In the ceramic phase the backfeeding rate stabilized due to the uniform nature of the ceramic at 0.9 mm/hr. The final crystal was just over 7 cm in length.

The second growth was started using the successful conditions of the first growth. A higher power setting was eventually needed, likely due to a slightly larger diameter of the rod and a slightly larger zone during this growth. The crystal was stabilized at 90.3 percent power at a growth rate of 1.5 mm/hr and was, at its best, stable for just under two hours at 90.2 percent power, followed by just over 14 hours at 90.3 percent power. At this point the material for the growth was exhausted. This second crystal was used primarily for the muon

experiments, and due to its size pieces have been reserved for examination by other condensed matter techniques.

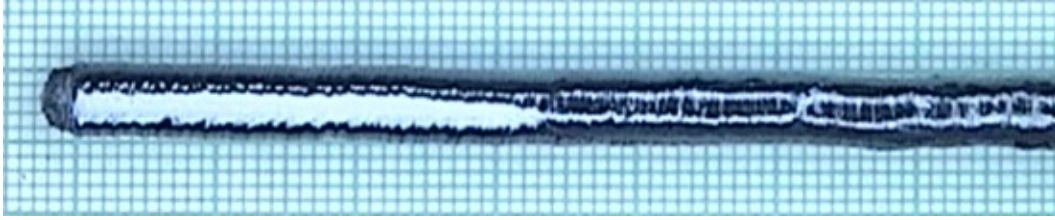


Figure 2.6: A Cobalt Niobate Crystal Grown in the Optical Floating Zone

2.4 SQUID Magnetometry

SQUID (Superconducting Quantum Interferometry Device) magnetometry was done on this sample along each crystallographic axis as a confirmation of the material as grown. The basic working principle of a SQUID magnetometer is as follows: a superconducting ring is formed and bridged on each side by two small non-superconducting contacts. The electric current between these two superconductors will depend on the phase difference, $\Delta\phi$, of the two wavefunctions, and will have a potential difference that is dependant on the time derivative of the phase difference. $\Delta\phi$ is additionally affected by the magnetic flux, Φ , through the ring. This type of structure can, therefore, convert magnetic flux into a voltage.

In the Quantum Design SQUID magnetometer, there is a Reciprocating Sample Oscillator, or RSO, which moves the sample up and down through a series of 4 pick-up coils, counter-wound in a A-B-B-A arrangement where the B loops are essentially co-located while the A loops are approximately 1.5 cm away from the B loops. This arrangement acts as a second order gradiometer.

Using Faraday's law, passing a magnetic material through a loop will induce a current, and the counter-wound loops will generate an oscillating response. The readout is then locked to the frequency of oscillation of the sample, and an extremely precise measurement of the magnetism of the sample can be obtained[24].

From measurements made by Prabhakaran[25] and Scharf[8] the expectation is that the spins are canted at 31 degrees in the a-c plane, and lie perpendicular to the b-axis. This means that we expect no magnetization, M , to be expressed along the b direction.

The sample was examined using similar runs to that performed by Prabhakaran[25] and Hanawa[3]. Each orientation was examined in the range where phase transitions were expected, focusing on the range from 1.8 K to 5 K, in a field of 100 Oe.

Additional measurements were taken in the $H \parallel b$ direction, again for comparison. In this case, the range from 1.8 K to 5 K was probed in 0.1 K steps, the range from 5 K to 10 K in 0.5 K steps, the range from 10 K to 50 K in 1 K steps and then up to room temperature (300 K) in 5 K steps. Three field scans from 0 to 2000 Oe in 50 Oe steps were performed at 1.8, 2.5 and 5 K.

The data provided was very similar, although unlike Scharf we see some activity in the $H \parallel b$ direction. This is common with Prabhakaran, although the magnetic peak that we see is at approximately 3.5 K, while Prabhakaran found his at 4.5 K. Additionally, our magnetic deviation is much smaller than that detected by Prabhakaran. We draw the similar conclusion that this pro-

portionally weak peak, as seen in figure 2.9, is likely due to the fact that the field is not perfectly parallel to the b-axis, and so although we do see some low temperature deviation, we would expect to see no temperature dependence at the low temperature scale of the susceptibility with field applied along the b-axis, other than the Curie-like behaviour exhibited in all three directions with increasing temperature. The non-zero portion of susceptibility with the field applied to the b-axis is due to effects such as core diamagnetism, which is the response of the inner orbitals to a magnetic field. A comparison of our data to Hanawa's data as a reference is shown in figures 2.7 and 2.7. A plot of our high temperature data is given in figure 2.9.

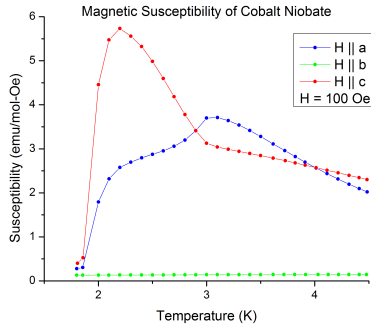


Figure 2.7: Magnetic Susceptibility of Cobalt Niobate Measured by SQUID Magnetometry

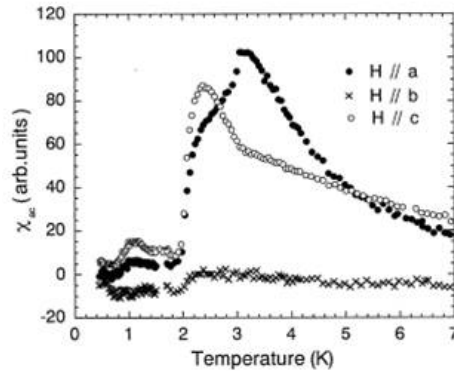


Figure 2.8: Cobalt Niobate Magnetic Susceptibility Measured by Hanawa[3]

From the behaviour shown by SQUID magnetometry, we can be confident that we do have a bulk single crystal, as well as samples aligned reasonably well along the b-axis for use in the μ SR and other experiments.

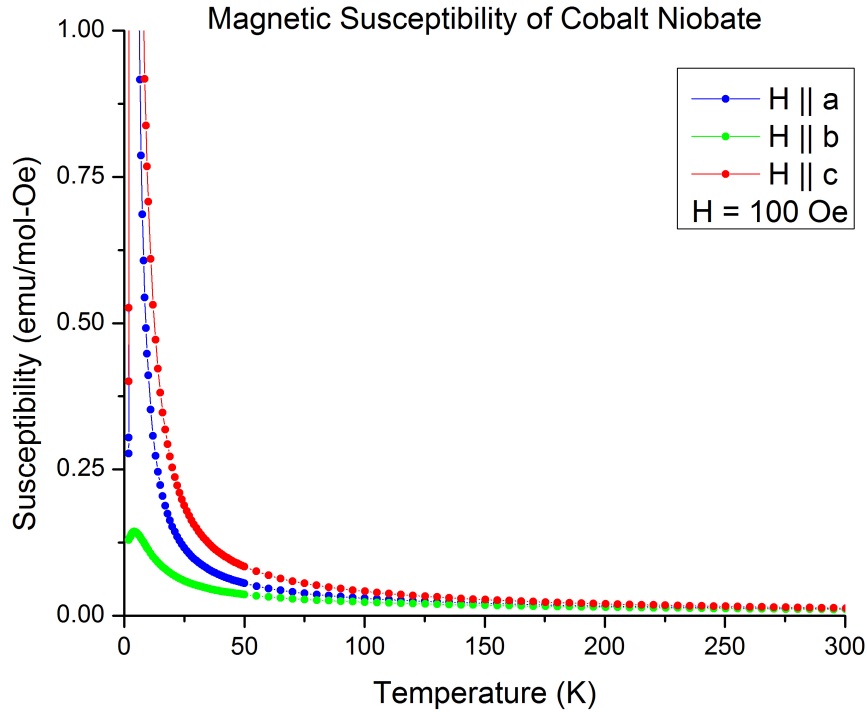


Figure 2.9: Magnetic Susceptibility of Cobalt Niobate up to 300 K at 100 Oe, Measured by SQUID Magnetometry

2.5 Sample Preparation

The data given by SQUID magnetometry emphasized the importance of proper alignment of the crystals. The desired direction to cut the material was so that the b-axis was perpendicular to the plane of the cut, or that the face of the crystal after being cut was the a-c plane. Using Laue diffraction the sample was aligned and then mounted using epoxy on a glass slide affixed to an aluminum block. Using a kerosene saw and diamond blade, the crystal was sliced along the b-axis in an area that was confirmed by Laue diffraction to be a single crystal on the surface. For the μ SR experiments described

further, 14 slices were cut with thicknesses of 0.5 ± 0.2 mm. Additionally, a block measuring 4.76 mm x 4.04 mm x 2.24 mm was cut and polished for future NMR experiments. The remainder of the crystal has been reserved for neutron scattering or other studies. Each of the square pieces were aligned so that the a-axis was in a known direction and glued to a plate. The edges of the crystals were then cut off, so that the crystals could be formed into squares for tiling. One of the 14 slices was cut into a 2.5 mm x 1.5 mm x 0.9 mm slice for heat capacity measurements. One of the surfaces of this piece was polished using a 1 micron grit silicon carbide slurry to ensure good thermal contact. See Figure 2.11 for an image just prior to the final cut of the bevelled edge. The darker area is the bevelled edge. The darkness is due to refraction of the light projected up from the light box. Additionally, the surface scratches are the result of the 1 μ m grit polishing. The samples were wrapped with Kim Wipe tissues and placed in labelled glass containers for transport. No other preparations or protections were required for these samples.

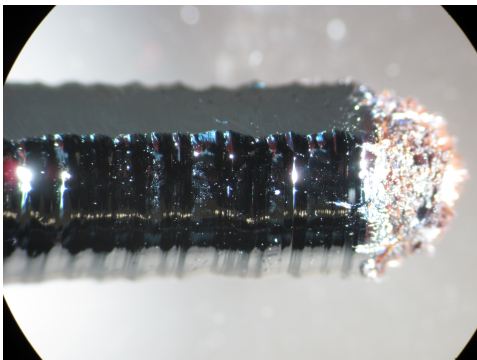


Figure 2.10: The Screw Dislocation During Growth

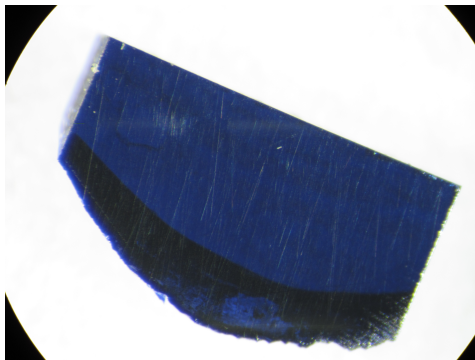


Figure 2.11: Prepared Slice for Specific Heat Measurements Before the Final Cut

Chapter 3

Low Temperature Specific Heat Measurements of CoNb_2O_6

3.1 Introduction to Specific Heat Measurements

Specific heat, $C(T)$, measurements are done to determine how quickly materials can adapt to thermal changes, and how they proceed through phase changes when they occur. Specifically it is related to the temperature change of a material, generally per mole, for a given amount of heat applied. First order transitions will exhibit some form of latent heat, where the material requires energy to change its structure while temperature remains constant. In materials with a second order phase transition, the transition is continuous so the effect happens concurrently. The entropy, or disorder of a system, cannot be measured directly, but using equation (3.1) it can be related to the specific heat of the system[26].

$$S(T) - S(T_0) = \int_{T_0}^T \frac{C(T')}{T'} dT' \quad (3.1)$$

To measure the specific heat of a material, the material will be placed in contact with a thermodynamic reservoir and allowed to come to equilibrium with that reservoir. The material then has heat added to itself directly, moving out of thermal equilibrium with the bath. The heat is added until the temperature of the sample being measured is constant at a value above the bath temperature. Nominally this is approximately 10 percent above the bath temperature. The heat source is then removed and the temperature change of the sample is monitored. The material will then lose heat through conduction, convection or other internal processes until it comes into thermal equilibrium with the bath. Since this is generally based on Newton's laws of cooling, Equations (3.2) & (3.3), we expect exponential behaviour of temperature with respect to time. What we find is that, especially at low temperatures, we can separate the different parts of the exponential decay into a sum of each component contributing to the total decay. From this we can extract the time constants of the material and determine exactly how long it takes for the system to relax.

$$\Delta Q = mC_P \Delta T \quad (3.2)$$

$$\frac{dT}{dt} = K(T - T_s) \quad (3.3)$$

Heat capacity measurement consist of several contributions. First, the heat capacity of the experimental components and glues used on the sample must be subtracted. These are generally experimentally known. For consideration in this experiment, we are looking primarily at the spin-spin and the phonon contributions. Thinking about the whole system as a series reservoirs, we have already established our external bath as a large reservoir, but within the material we can have several different, smaller reservoirs. The spin-spin reservoir would be representative of the interaction energy between magnetic moments, such as the exchange energy or dipolar terms. This spin-spin reservoir can actually be a collection of multiple reservoirs of different spin sublattices. The phonon reservoir would be representative of the energy of the phonons and is also the reservoir that would be considered to be in primary contact with the external reservoir. Additionally, we must consider the system having a Zeeman heat capacity to represent the energy imparted to the spins on the lattice by a static field wherever the measurements of heat capacity are not performed in zero field[27]. Of importance is that the time constants for each material are temperature and phase dependent and that they are also all interlinked. At higher temperatures, the phonon contribution dominates due to the T^3 nature of the Debye term (3.4)[28]. At lower temperatures, other terms can dominate, especially given that experimentally we see a long coupling constant between the spin and phonon terms.

$$C_V = \left(\frac{\partial U}{\partial T} \right)_V = \frac{12\pi^4 N k_b}{5} \left(\frac{T}{\theta} \right)^3 \quad (3.4)$$

3.2 Room Temperature to 2 Kelvin

The high temperature measurements were performed on an Oxford Instruments ExaLab. A piece of cobalt niobate was cut and polished as described in Chapter 2. The piece was carefully weighed and then had 40 μg of Apiezon N grease applied to the polished side. This was then placed on the sapphire chip on the heat capacity probe. The grease was added to ensure good thermal contact as well as to prevent the sample from moving. The polishing of the surface was done for the same reason. The sapphire chip is suspended by an array of weak link wires that create a connection characterized by low thermal resistance. The design of the heat capacity probe is such that the variable temperature bath of gaseous helium is in direct, mechanical contact with the copper frame of the probe. The copper frame has the weak link wires directly attached.

The Oxford Instruments software was used to capture the data in an automated fashion. The software determines the heat pulse size needed automatically, heats the sample to the required level and monitors until the sample is at equilibrium with the bath. The parameters for removing the heat capacity contributions of the sapphire chip as well as the Apiezon grease are coded into the analysis and removed automatically. The method used by the software is the temperature relaxation method. In this method the material is allowed to come to equilibrium with the external environment. Heat is then applied to the system until the material is at a temperature differential away from the thermal bath, as computed by the software. It is then allowed to cool in the heat bath, having its temperature measured constantly by a Cernox resistor

within the heat capacity probe, until the material is once again in thermal equilibrium with the bath.

From our measurements we can determine that the sample quality is quite good, and we have also shown that our data confirms that of the previous work on cobalt niobate done by Hanawa et al.[3] The Hanawa et al. data extends down to 600 mK. From the data we can see the expected, characteristic decay of heat capacity, at all probed fields, as well as indications of one of the expected magnetic phase changes through the peak at approximately 2.9 K corresponding to expectations from work by Heid et al.[11][12] and Mitsuda et al.[6]. That we see a smooth heat capacity curve, as opposed to this abrupt peak, with an applied field may be because the field changes the type of ordering experiences at the transition from a paramagnetic to incommensurate phase to one that is a paramagnetic to spin-flip phase[11]. This can be seen in Figure 3.1. Further low field measurements are planned to interpolate the 0 T to 0.2 T region to try and determine the mechanism that takes the sharp peak and flattens it into a broad peak with a protracted tail.

Looking at changing fields below the transition temperature in Figure 3.2, we find that as we get closer to the peak itself, we see a sharpening of the peak, as well as a shift of the peak to the higher fields. From the temperature plot we see that the die-off of the peak is quite sharp at higher temperatures. This data, taken as a set, shows us a good representation of the phase boundary in temperature and field space. Of note, the linear shift down in the 2.3 K data as well as the different values of the 2.8 K runs with increasing field was due to tolerances set in the computer data acquisition program. In the case of the

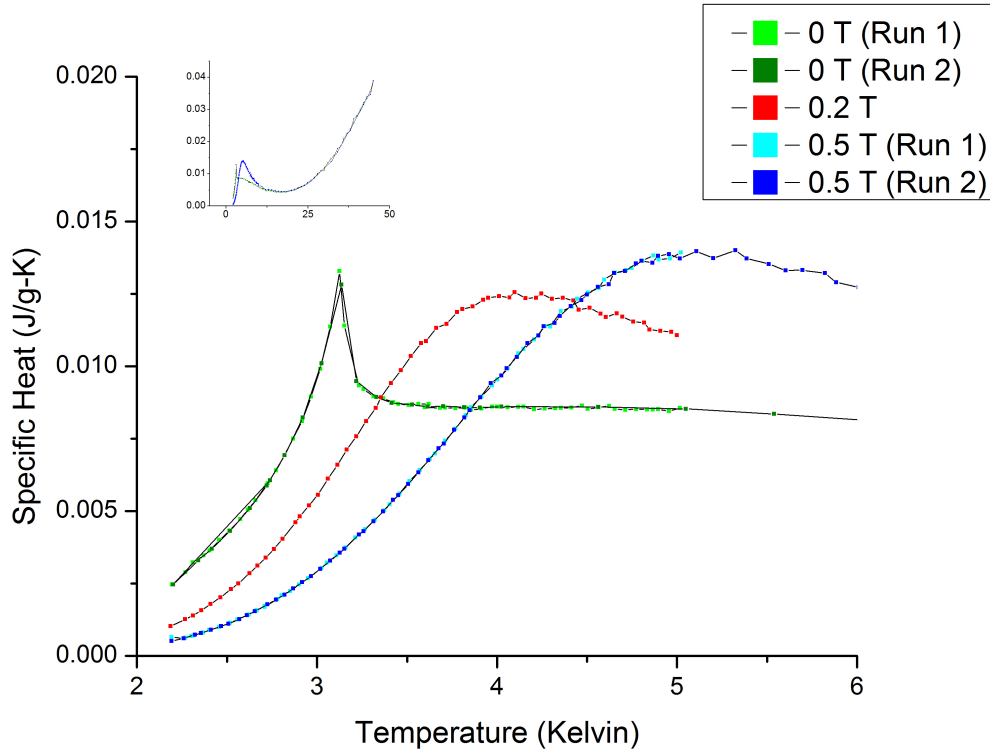


Figure 3.1: Plot of Specific Heat versus temperature at Varying Fields. Inset up to 45 K.

linear shift the program stopped running and the sample cooled from 2.35 K, the upper range of the temperature tolerance, to 2.25 K, the lower tolerance limit, before the run could be resumed. The abrupt discontinuity is evident in the data, but it is not a real effect. The difference in the 2.8 K runs is for a similar reason. Observing the plot, it is easy to see a strong temperature dependence.

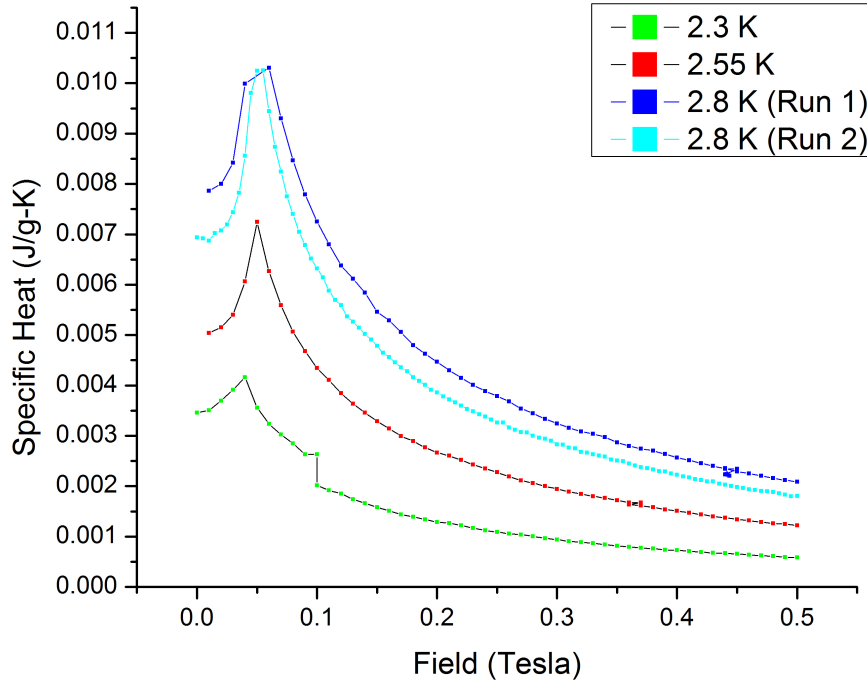


Figure 3.2: Plot of Specific Heat versus Field at Varying Temperatures below the 2.9K transition

3.3 Below 2 Kelvin

To examine below the temperature range possible with the ExaLab, measurements at cryogenic temperatures were performed at the University of Waterloo on small pieces of cobalt niobate prepared from the same crystal. In the Waterloo setup, the sample is connected by a thermal weak link, which is a material with a long time constant. In this case a wire of manganin was used. The wire was glued to the surface of the cobalt niobate, which instead of being placed on a sapphire plate, was suspended instead by nylon wires. The measurements done were performed utilizing the thermal relaxation method

described above. The most important feature of this method of measurement is the long duration spent allowing the material to sit at equilibrium. The importance of this point is that it allows for the thermal energy to get into the magnetic spin subsystem. This ensures that contributions due to the contribution of magnetism to specific heat are neither overlooked nor underestimated.

The decay plot from the cobalt niobate sample showed a very quick decay for the manganin-related term, as well as an increasingly long tail. At present the data set has been fit to multiple exponentials. The first is a very short decay which is attributable to the τ_2 contribution from the connection between the microcalorimeter and the sample. The second is a decay due to the connection to the weak link itself. Both of these need to be subtracted from the system. The latter would be representative of the material if there wasn't a third exponential with an exceptionally long time constant. This is presently believed to be a "phonon bottleneck" where the energy is taking a longer time to move from the magnetic spin subsystem to the crystal lattice as phonons which would drain through the weak link. To understand this mechanism further a microscopic model would need to be developed. At present, the lowest measurements performed have been done down to 330 mK. This final data point may indicate a phase transition, however there is a large amount of noise at the lowest temperatures due to the system itself. The dewer currently in use can only maintain thermal stability for two days, which is not enough time to measure a complete thermal relaxation curve at temperatures below 330 mK. The cryogenics lab in Waterloo is procuring a dewer that can hold up to a weeks worth of helium, at which point the lower temperature dynamics can be further examined.

The important result at this point in time from the low temperature data is the exceptionally long and exponentially increasing relaxation time of the lattice at very low temperatures. This leads to an interesting question on data collected by other techniques in attempting to probe the lowest temperatures of the cobalt niobate phase diagram: was the system in its final state when the measurements were taken? Above 1 K we find the relaxation time is on the order of minutes. However, below 500 mK we see this rate increasing to the order of hours or days, if the relaxation time plot turns out to be extrapolatable. A plot of the specific heat as well of the internal time constant is given in Figure 3.3.

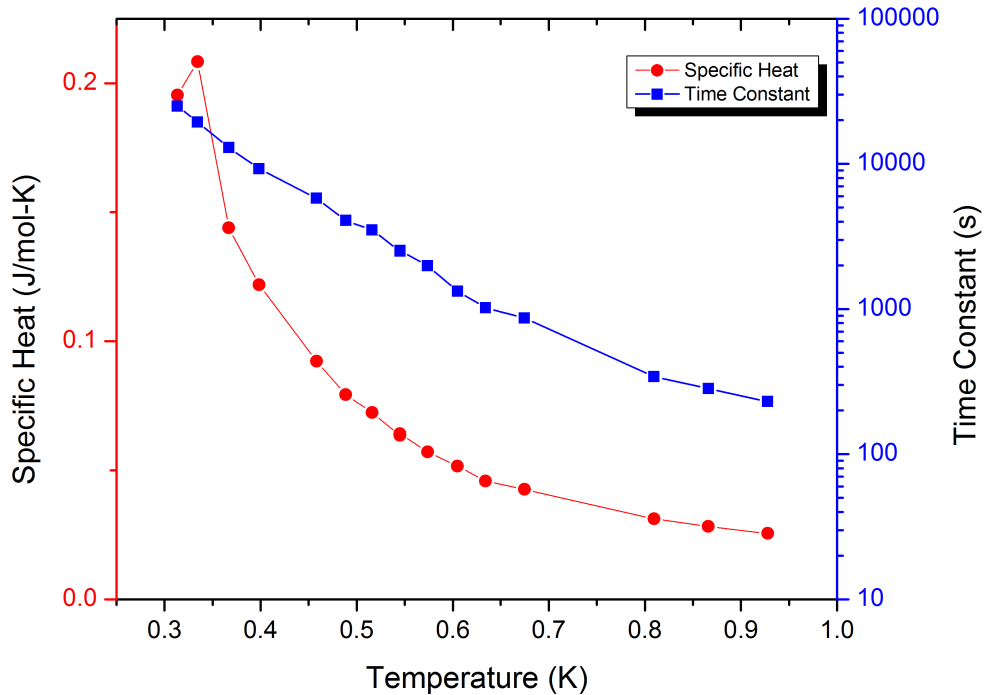


Figure 3.3: Specific Heat Capacity and Relaxation Time Constant below 1 K

Although there is a gap in the data between 1 K and 2.2 K, the data we have collected fits well with the prior data in literature. No large deviation is seen at the 1.9 K transition, although confirming this to complete the picture is a future goal. The data set can be seen in Figure 3.4. In addition, we have also looked at a C/T versus T^2 as an alternative plot to visualize the phonon contribution to the heat capacity. We see from Figure 3.5 that the phonon contribution only seems to become the dominant term around 20 K, meaning that the low temperature physics are dominated by other processes. If the linear trend of Figure 3.5 were extended it would go to zero at zero temperature, as expected for the phonon contribution. In a typical metal the T^3 phonon component would generally be dominant to a far lower temperature than 20 K.

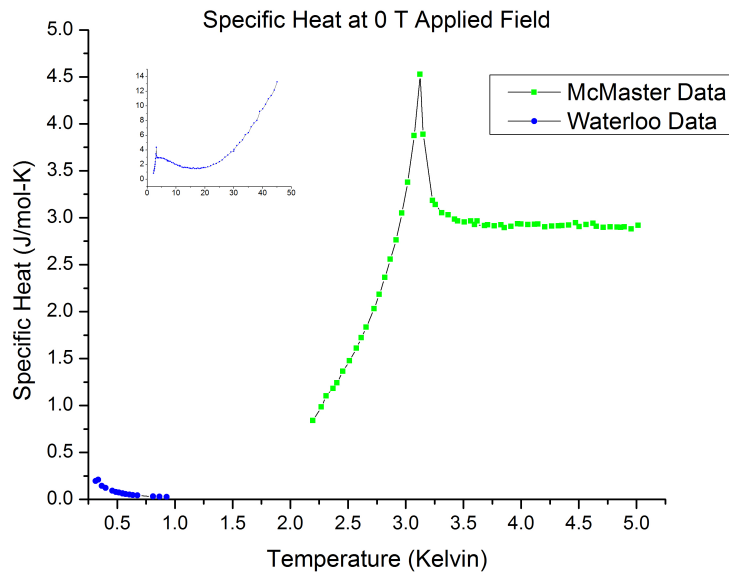


Figure 3.4: Low and High Temperature Specific Heat of Cobalt Niobate (Inset axes have the same labels)

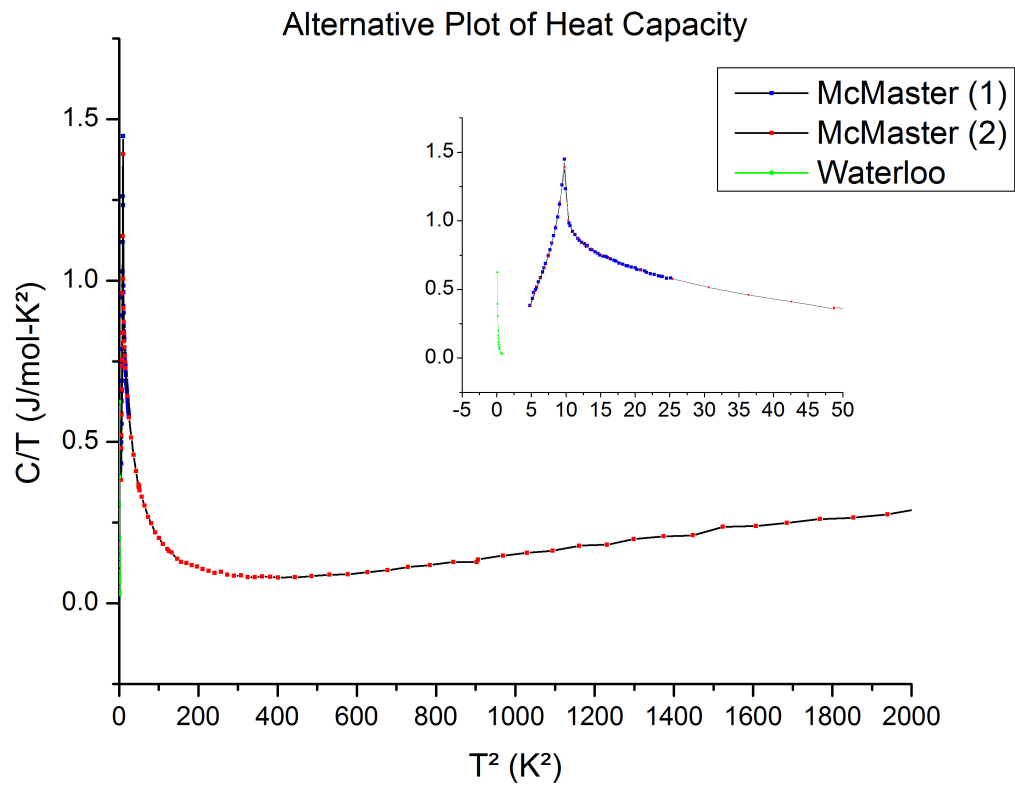


Figure 3.5: Alternative Heat Capacity Plot of Cobalt Niobate

Chapter 4

Muon Spin Rotation Theory

4.1 Introduction to Muon Spin Rotation

Muon spin rotation (more properly the combined techniques of muons spin rotation, relaxation and resonance), or μ SR, is the most sensitive local probe of magnetism for condensed matter systems. These methods consists of implanting spin-polarized muons into a sample and trying to determine the effects of the local environment on the muon. The following paragraphs give an introduction to muon creation and implantation and are followed by an examination of three different methods of performing a μ SR experiment.

4.1.1 Pion Production and Decay

Muons in nature exist ambiently, most commonly as a byproduct of cosmic energy ray interactions in the upper atmosphere. The flux of cosmic ray muons, however, is so small that for the generally large statistics required for an experiment, a direct, as opposed to ambient, source is necessary. Cosmic ray muons have been used recently for experimentation, an interesting example

of which was attempting to map the interiors of Mexican pyramids, looking for hidden burial passages[29]. However, from the referenced article, they measured a million muons over the course of months. For practical condensed matter experiments, we require the same number of muons on a timescale on the order of minutes.

Muons can be created from one of the decay channels of the pion. The pion, or π -meson, can be created by bombarding nucleonic particles. For the generation of pions in this experiment, this was done by using a proton beam. At TRIUMF in Vancouver, a large cyclotron is injected with H^- ions, accelerating them to ~ 500 MeV. After approximately 1500 revolutions, the electrons are stripped using a carbon foil and the protons are and extracted down a beamline. To generate pions, these high energy protons are impacted into a target made with a material with a low atomic number (Z), such as Carbon or Beryllium. Pions are typically generated by the following mechanisms, although higher-energy decay channels exist as well.

$$p + n \Rightarrow p + n + \pi^0$$

$$p + n \Rightarrow p + p + \pi^-$$

$$p + n \Rightarrow p + n + \pi^+$$

Pions are unstable particles and have a decay lifetime of approximately 26 ns. The decay modes of each type of pion into a muon are as follows:

$$\pi^0 \Rightarrow \gamma + \gamma$$

$$\pi^- \Rightarrow \mu^- + \bar{\nu}_\mu$$

$$\pi^+ \Rightarrow \mu^+ + \nu_\mu$$

It is possible for a pion to decay into an electron and electron neutrino pair, however, the branching ratio between these two decay channels can be theoretically computed using Equation (4.1), which shows an overwhelming preference for the pion to decay into the muon[30].

$$\frac{\Gamma(\pi^- \rightarrow e^- + \bar{\nu}_e)}{\Gamma(\pi^- \rightarrow \mu^- + \bar{\nu}_\mu)} = 1.28 \times 10^4 \quad (4.1)$$

Some low energy pions have insufficient energy to escape the production target, and are considered to be pions at rest. The muons created from this pion decay are surface muons with 4.119 MeV of kinetic energy and are 100 % spin polarized. This is because the pion is a spin-0 particle, while the muon and the anti-neutrino are spin-1/2. Therefore, due to the conservation laws and the fact that anti-neutrinos are right-handed, the muons generated must be left-handed[30].

Additionally, any of the μ^- particles created are quickly captured by nuclei in the production target, so for the purpose of the experiments done in this thesis, only μ^+ muons are considered. Generation of a beam of μ^- is possible by having higher energy pions, but the pion decay will not be at rest in the production target, so they will be required to decay in flight and therefore will also not be 100% spin polarized.

4.1.2 Muon Production and Decay

The muon that emerges from the pion decay in the rest frame will have a momentum of 29.79 MeV/c and will have a kinetic energy of 4.119 MeV.

Because the pion decay is a two-body decay involving one anti-neutrino and the muon there is no variation in this output.

The positive muon is a weakly interacting spin-1/2 member of the lepton family. Its interactions can be described like those of an electron, however, with a mass that is approximately one ninth of a proton. Due to the mass and corresponding gyromagnetic ratio, it behaves very similarly to a proton. The properties of a muon, proton and electron are compared in Table 4.1.

Particle	μ^+	p^+	e^-
Lifetime	2.19698 μs	$> 2.1 \times 10^{29}$ years	$> 4.6 \times 10^{26}$ years
Spin	1/2	1/2	1/2
Mass [MeV]	105.658	938.272	0.511
Gyromagnetic Ratio (γ) [(sT) $^{-1}$]	8.516154×10^8	2.67522×10^8	1.76086×10^{11}
Larmor Frequency ($\gamma/2\pi$)[MHz/T]	135.54	42.58	28,024.95

Table 4.1: Comparison of the Characteristics of the Muon, Proton and Electron[31][32]

Since muons are charged particles, they can be steered by magnetic and electric fields. At TRIUMF, there are dipole magnets, which are used for selecting muon momentum and quadrupole magnets which are used to focus the muon beam. The beamline includes Wien filters prior to the sample which have electric and magnetic fields tuned to the charge to mass ratio of the muon. This is to remove any other particles from the beam before it is incident with the sample. In the case of the beamline at TRIUMF these contaminants are primarily positrons.

μSR is a local probe, and in most experiments the stopping depth of the muon is not a key consideration. For the surface muons referenced above, the

depth that muons will penetrate, R , can be converted into a stopping distance by multiplying by the sample density, which for a typical sample will give a value of $R\rho \approx 110mg/cm^2$, so muon penetration is generally between 0.1 and 1 mm.

Once a muon is at rest in the local sample environment, because it is a charged spin-1/2 particle, it will precess in the local magnetic field with a frequency of $\omega = \gamma_\mu B_{loc}$. The positive muon will decay as follows:

$$\mu^+ \rightarrow e^+ + \nu_e + \bar{\nu}_\mu$$

For completeness, the negative muon decays as follows:

$$\mu^- \rightarrow e^- + \bar{\nu}_e + \nu_\mu$$

In this case we have a three-body final state decay, so the exiting positron will not have an exact energy or momentum, as the muon does after pion decay[30]. Instead, the positron will be emitted only preferentially in the direction that the muon spin was pointed when it decayed. The emission probability is given by integrating over the neutrino momenta, and is given by the following derivation[33][34]:

$$d^2W = W(\theta, \epsilon)d\epsilon d(\cos \theta) \tag{4.2}$$

$$= \frac{G^2 m_\mu^5}{192\pi^3} \times (3 - 2\epsilon)\epsilon^2 \left[1 + \frac{(2\epsilon - 1)}{3 - 2\epsilon} \cos \theta \right] d\epsilon d(\cos \theta) \tag{4.3}$$

Integrating over $\cos \theta$

$$dW(\epsilon) = W(\epsilon)d\epsilon = \frac{2(3 - 2\epsilon)\epsilon^2}{\tau_\mu} \quad (4.4)$$

where	W		is the decay distribution of the positron
	τ_μ	$= \frac{192\pi^3}{G^2 m_\mu^5}$	Average muon lifetime (2.19698 μ s)
	G_μ	$= 1.16637 \times 10^{-5} GeV^{-2}$	Fermi electroweak coupling constant
	m_μ	$= 105.658 \text{ MeV}$	Muon rest mass
	$a(\epsilon)$	$= \frac{2\epsilon - 1}{3 - 2\epsilon} \times P$	asymmetry factor for a given polarization
	ϵ	$= \frac{E}{E_{max}}$	
	E_{max}	$= 52.83 \text{ MeV}$	Maximum energy of a decay positron
	θ		Angle between muon spin and direction of positron emission

Figure 4.1 shows the probability of direction of positron emission when a muon decays with the spin prior to decay represented by the arrow. The red circle is representative of the average over all positron energies, while the blue cardioid represents the scenario of all positrons emitted at the maximum energy.

Although neither the neutrino nor the antineutrino are easily detectable, the positron is. Scintillators attached to photomultipliers are used as detectors and are positioned around the sample in geometries dependant on the magnetic field, the incident beam and the desired measurement. The distribution of the decay muons is asymmetric with respect to the muon polarization vector, $P(t)$.

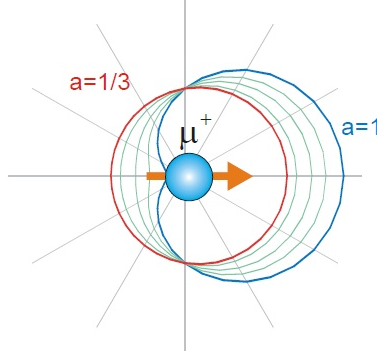


Figure 4.1: Probability of Direction of Emission of the Positron upon Muon Decay (Taken from Reference [35])

Since the probability of emission of the positron is highest along the direction of muon spin, by monitoring the polarization vector we extract the information about the spin direction at the time of muon decay. The whole system is electronically gated so that only a single muon at a time is in the sample, and therefore each decay should be from a known muon. This is important because since the statistics and the precession are time dependent, if there were muons entering the sample continuously it would be impossible to match a muon with its decay to extract a time, and therefore be confident in $P(t)$.

We can determine the number of decay positrons, $N_i(t)$, recorded per time bin using Equation (4.5). The time evolution of the muon polarization function is given by Equation (4.6)[36].

$$N_i(t) = N_i^0 e^{-t/\tau_\mu} [1 + A_i^0 P_i(t)] + B_i^0 \quad (4.5)$$

where N_i^0 is a normalization constant
 A_i^0 is the maximum precession amplitude, or the intrinsic asymmetry of the positron detector
 $P_i(t)$ is the time evolution of the muons spin polarization (eqn (4.6))
 B_i^0 is a time independent random background

$$P_i(t) = \cos(\omega_\mu t + \theta_i) \tag{4.6}$$

where θ_i is the initial phase of the muon spin polarization vector.

The initial phase of the muon polarization function, θ_i , is generally non-zero because muons will precess in the flight to the sample, due to contributions from the magnetic field being generated between the muon gate counter and the sample itself. There is, however, no significant change during muon thermalization because the muons typically lose their initial kinetic energy through electrostatic interactions with the material, which will not significantly affect the spin[37]. In a typical μ SR experiment the signal-to-noise ratio is proportional to $A_i^0 \sqrt{N_i^0}$ [38].

Additionally, Equation (4.5) is applicable to each independent counter and due to construction and misalignment can have different values of A^0 and B^0 . Note that an opposing counter would be expected to have a negative sign in place of a positive sign in front of the maximum precession amplitude. For a forward-back counter pair, we can combine the counts into a total asymmetry function as follows:

$$N_F(t) = N_F^0 e^{(-t/\tau_\mu)} [1 + A_F(t)G_z(t)] \quad (4.7)$$

$$N_B(t) = N_B^0 e^{(-t/\tau_\mu)} [1 - A_B(t)G_z(t)] \quad (4.8)$$

$$A_F G_z(t) = \frac{\alpha N_F(t) - N_B(t)}{\alpha \beta N_F(t) - N_B(t)} \quad (4.9)$$

$$\text{where } \alpha = \frac{N_B^0}{N_F^0}$$

$$\beta = \frac{A_B}{A_F}$$

The α parameter corrects for differences in the solid angle exposed to the detector, the efficiency difference between the two counters and the parameters of beam intensity and delivery. The parameter α can be fit experimentally by doing a calibration using a weak transverse field. Typically field strengths in the range of 20 to 100 G are used to create the data set to fit for this correction. The β parameter is the correction for the difference in counter asymmetry and is based on the construction of the detectors. β is expected to be very close to 1, a value that is generally assumed in data analysis.

4.1.3 Muon Spin Rotation and Relaxation as a Probe of Local Magnetism

When describing μ SR, it is easiest to think of the measurements of local magnetism based on the field being applied. In the case of a field in the transverse direction, or perpendicular to the initial polarization, the term muon spin rotation is best applied, as the effect that is being probed is the preces-

sion based on the difference between the applied field and the dipolar moments of the atoms near the muon site. The field will cause a precession proportional to the size of the moment at the muon site, which will be detectable as a periodicity in the asymmetry plots (See Equation (4.9)). Conversely, when we are talking about longitudinal fields, our field is aligned with the spin so rather than talking about rotation and precession, it is actually the relaxation rate of the spin that is being probed, or the time evolution of the muon polarization function.

4.2 Zero and Longitudinal Field μ SR

Both zero field measurements and longitudinal field measurements of μ SR are typically set up and analyzed in the same way. The spins in zero field can be rotated 90 degrees using Wien filters to give the muons a different initial polarization so that the effects of implantation along different crystal directions can be easily observed. A weak field parallel to the Earth's magnetic field may be applied to screen that small contribution out, to get a true zero field in the sample.

Longitudinal relaxation, in the case of μ SR, refers to a magnetic field that is parallel to the initial muon polarization, which is parallel to the beam direction. Since there is no appreciable transverse magnetic field from when the muon is generated to sample implantation, the muons should land with their initial spin polarization intact. The relaxation function extracted from longitudinal μ SR measurements gives information about the time evolution of the polarization parallel to the initial spin direction.

To perform both zero and longitudinal field measurements, typically a forward and a back counter are utilized, which would ideally be placed at 0 and 180 degrees from the incident beam. The longitudinal relaxation function can be obtained from either the forward or back counter histogram independently; however in general a sum and difference ratio is taken. The useful information, in this case, comes from the form and the magnitude of the relaxation rate of the muon. Denoting the forward counter as $F(t)$ [Equation (4.10)], the back counter as $B(t)$ [Equation (4.11)]:

$$F(t) \propto e^{(-t/\tau_\mu)}(1 + A_F P_z(t)) \quad (4.10)$$

$$B(t) \propto e^{(-t/\tau_\mu)}(1 - A_B P_z(t)) \quad (4.11)$$

The spin polarization of the muon, $\sigma_z(t)$, can be expressed as shown in Figure 4.2 and Equation (4.12). The first term refers to the average time-independent polarization along the direction of spin polarization while the second term precesses as a frequency $\gamma_\mu B$. The angle θ is measured between the spin polarization direction and the direction of the field.

$$\sigma_z(t) = \cos^2 \theta + \sin^2 \theta \cos(\gamma_\mu B t) \quad (4.12)$$

$$(4.13)$$

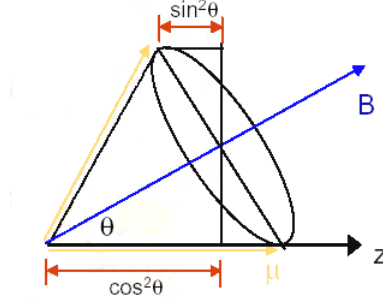


Figure 4.2: A Schematic of Muon Precession around the Internal Magnetic Field (Adapted from [39])

4.2.1 Static Magnetism

The muon spin relaxation function, $G_z(t)$, can be obtained by averaging $\sigma_z(t)$ over the sphere, and is the starting point of determining the relaxation functions. The integral form of the muon spin relaxation function is given in Equation (4.14). Performing a time average on this equation over the sphere converts the cosine squared into a value of $\frac{1}{3}$ and the sine squared into a value of $\frac{2}{3}$ [40].

$$G_z(t) = \iiint \sigma_z(t) P(B_x) P(B_y) P(B_z) dB_x dB_y dB_z \quad (4.14)$$

If we assume the case of a system with concentrated dipole moments, such as in the case of nuclear dipoles, the probability distribution, $P(B)$, is modelled as a Gaussian distribution function (Equation (4.15)). In the case of dilute magnetic moments, the probability distribution is better modelled as a Lorentzian distribution function (Equation (4.16))[41].

$$P^G(B_i) = \frac{\gamma_\mu}{\sqrt{2\pi}\Delta} e^{-\frac{\gamma_\mu^2 B_i^2}{2\Delta^2}} \quad (4.15)$$

$$P^L(B_i) = \frac{\gamma_\mu}{\pi} \frac{a}{a^2 + \gamma_\mu^2 B_i^2} \quad (4.16)$$

where γ_μ is the precession rate
 $\gamma_\mu B$ = ω , the precession frequency
 Δ/ω is the FWHM of the Gaussian Distribution
 a = $\Lambda\gamma_\mu$
 Λ is the FWHM of the Lorentzian Distribution
 $i \in \{x,y,z\}$

We can evaluate the integrals in both cases and can solve the relaxation function for the Gaussian and Lorentzian cases, which are given in Equations (4.17) and (4.18) respectively. These functions are known as the zero field Kubo-Toyabe functions. The $\frac{2}{3}$ components are expected to have their spins depolarize at the rates of either $\frac{1}{\Delta}$ for the Gaussian case or $\frac{1}{a}$ for the Lorentzian case.

$$G_z^G(t) = \frac{1}{3} + \frac{2}{3}(1 - \Delta^2 t^2) e^{-\frac{\Delta^2 t^2}{2}} \quad (4.17)$$

$$G_z^L(t) = \frac{1}{3} + \frac{2}{3}(1 - at) e^{-at} \quad (4.18)$$

If we now apply a longitudinal field, we should cause the Kubo-Toyabe functions to recover to a flattened asymmetry. Before we perform the integration, we are changing the probability distribution in the z direction by an

offset of B_{ext} , the applied longitudinal field. The probabilities for the Gaussian and Lorentzian cases are given in Equations (4.19) and (4.20).

$$P^G(B_z) = \frac{\gamma_\mu}{\sqrt{2\pi}\Delta} e^{-\frac{\gamma_\mu^2(B_z - B_{ext})^2}{2\Delta^2}} \quad (4.19)$$

$$P^L(B_z) = \frac{\gamma_\mu}{\pi} \frac{a}{a^2 + \gamma_\mu^2(B_z - B_{ext})^2} \quad (4.20)$$

These functions, when integrated, give the analytical solutions as shown in Equations (4.21) and (4.22). As the values of Δ/ω_{LF} and a/ω_{LF} tend to zero in the Gaussian or Lorentzian cases, the terms other than the leading 1 in the relaxation rate both tend to zero.

$$\begin{aligned} G_{LF}^G(t) = & 1 - \frac{2\Delta^2}{\omega_{LF}^2} \left[1 - e^{-\frac{\Delta^2 t^2}{2}} \cos(\omega_{LF} t) \right] \\ & + \frac{2\Delta^4}{\omega_{LF}^3} \int_0^t e^{-\frac{\Delta^2 \tau^2}{2}} \sin(\omega_{LF} \tau) d\tau \end{aligned} \quad (4.21)$$

$$\begin{aligned} G_{LF}^L(t) = & 1 - \frac{a}{\omega_{LF}} j_1(\omega_{LF} t) e^{-at} - \frac{a^2}{\omega_{LF}^2} [j_0(\omega_{LF} t) e^{-at} - 1] \\ & - \left[1 + \frac{a^2}{\omega_{LF}^2} \right] a \int_0^t j_0(\omega_{LF} \tau) e^{-a\tau} d\tau \end{aligned} \quad (4.22)$$

where j_0 and j_1 are spherical Bessel functions.

4.2.2 Dynamic Magnetism

In a dynamic case we assume the strong collision approximation. During the evolution of the muon precession, by assuming Brownian motion we expect each step to occur with a rate of $\omega_0\tau$, where ω_0 is $\gamma_\mu B$. We can define the relaxation time, T_1 , as the time it takes for a deviation of the phase by one radian. The relaxation rate, $1/T_1 \propto \omega_0^2\tau = \frac{\omega_0^2}{\nu}$ where ν represents the fluctuation rate. Larger fluctuation rates imply a better averaging of the randomness of the local field which results in a smaller relaxation rate[33].

The strong collision approximation assumes that the probability of collisions, $\rho(t)$ is $1 - e^{-\nu t}$. If we assume a Gaussian distribution with zero external field applied, we can determine the probabilities of collisions as:

Collisions	Probability
None	$e^{-\nu t} G_{Static}^G(t)$
One	$\nu \int_0^t G_{Static}^G(t_1) G_{Static}^G(t - t_1) dt$
Two	$\nu^2 \int_0^t \int_0^{t_2} G_{Static}^G(t_1) G_{Static}^G(t_2 - t_1) G_{Static}^G(t - t_2) dt_1 dt_2$

The table above continues for the decreasing probabilities of further collisions within the specified time interval. Summing all of these probabilities together creates a convolution integral, which can be solved by use of a Laplacian transformation[40].

In the limit where collisions are assumed to be slow, or where $\nu\Delta \ll 1$, we obtain the result given in Equation (4.23). For fast fluctuation, when $\nu\Delta \gtrsim 5$, the solution is given in Equation (4.24). In these regimes the slow limit sees a decay of the $1/3$ tail, while in the fast limit it is entirely gone and is

simply an exponential decay. In the case of fast relaxation the same process can be used for a Lorentzian distribution, although Gaussian collisions are still generally assumed as part of the strong collision approximation model. In this case, the power of the exponential changes, and is given in Equation (4.25). These equations form the basis of using a stretched exponential form to model systems. This generally shows that a stretched exponential should fit almost any dynamic function.

$$G_{Dyn(slow)}^G = \frac{1}{3} e^{-\frac{2}{3}\nu t} \quad (4.23)$$

$$G_{Dyn(fast)}^G = e^{-\frac{2\Delta^2 t}{\nu}} \quad (4.24)$$

$$G_{Dyn}^L = e^{-\sqrt{\frac{4a^2 t}{\nu}}} \quad (4.25)$$

With static local fields, we would expect that we will see a decoupling or separation of the longitudinal fields as the spins depolarize, compared to zero field value. This case requires that $\omega_{LF} \gg \Delta$. In the case of fast dynamic local fields, we find that the longitudinal and zero fields are almost identical and there is little dependence on the longitudinal field[33].

4.2.3 Overall Remarks

This section describes the experimental information necessary to distinguish between static and dynamic magnetism. In particular, zero field μ SR

can detect very slow fluctuations that would be too small to be detected by transverse field oscillations[37], which are described in the following section. Zero field μ SR is the most sensitive probe to test if there are static magnetic fields present. If no static moments are detected then the spins in the sample will not have frozen, and so the system must either be fluctuating or in a singlet ground state[35].

If the applied longitudinal field is strong enough to decouple the local hyperfine or dipolar fields, Equation (4.24) describes the relaxation of the Zeeman energy of the muon, which would be like the T_1 relaxation found using NMR. Since muons have a short lifetime, the relaxation that can be detected is on a relatively fast time scale and can be used to observe the fluctuations in the local moments[37].

4.3 Transverse Field μ SR

Transverse field muon spin rotation refers to the precession of the muon spin by a magnetic field that is perpendicular to the initial muon polarization, which is also perpendicular to the beam direction. There is a small distance where the muon could be affected and start to precess in the field prior to sample implantation, but the time of flight where the muon would be exposed outside of this sample is negligible. Additionally, this perturbation is also applied equally to every muon prior to sample implantation so all muons enter the sample with the same initial polarization. The asymmetry signal from a transverse field measurement is useful in determining the field distribution in the superconducting state as well as identifying magnetic domains in metals.

Additionally it is useful in determining the local magnetic susceptibility of the material under study[42].

The distribution of static fields is generally modelled as either with a Gaussian or a Lorentzian line shape forming the envelope of oscillation. The field distribution leads to a dephasing of the muon spins, which is responsible for the depolarization[42]. The form of the corrected asymmetry would be the form shown in Equation (4.26), where Δ_x is the damping factor.

$$G_x(t) = e^{-\frac{1}{2}\Delta_x^2 t^2} \quad (4.26)$$

For the case of a dynamic local field, the depolarization function depends on the fluctuation rate. In the case where the fluctuation rate is rapid, or $\tau_c \Delta_x \ll 1$, the corrected asymmetry can be represented by Equation (4.27) where τ_c represents the correlation time, or the inverse fluctuation rate. This equation is typically rewritten as Equation (4.28), where λ represents a damping factor, or where T_2 represents the transverse relaxation time.

$$G_x(t) = e^{-\Delta_x^2 \tau_c t} \quad (4.27)$$

$$G_x(t) = e^{-\lambda t} = -\frac{t}{T_2} \quad (4.28)$$

In the intermediate case between slow and fast relaxation, we get the Abragam lineshape, which is described in Equation (4.29). It is difficult to extract accurate fluctuation rates from a region of slow transverse field oscilla-

tion, so in these cases longitudinal or zero field measurements are much more advantageous to perform[34].

$$G_x(t) = e^{-\Delta_x^2 \tau_c^2 [e^{-(t/\tau_c)} - 1 + (t/\tau_c)]} \quad (4.29)$$

Within the envelope we typically have a cosine term to fit the precession of the polarization, so we get equations in the form of Equation (4.30)[42].

$$A(t) = G_x(t) \cos(\omega_{site} t) \quad (4.30)$$

It is possible for there to be several coexisting frequencies within the transverse field asymmetry envelope. In this case they can each be deconvolved and would each represent a distinct local field. These different fields typically exist either as inequivalent muon implantation sites or different magnetic domains within the material.

Chapter 5

Muons Spin Rotation Measurements of Cobalt Niobate

5.1 Facilities

As was stated in chapter 4, the μ SR were performed at TRIUMF, located on the south end of the campus of UBC in Vancouver. The accelerator at TRIUMF is a six-segment, continuous, medium-energy cyclotron. The cyclotron is capable of accelerating protons up to 520 MeV. A hydrogen atom has an extra electron added to fill its outer shell and give it an overall charge of $-e$. The hydrogen anion is steered into the cyclotron magnetically. The cyclotron contains a static magnetic field which holds the accelerating particles to a spiral pattern as well as an RF electric field which is used to accelerate the ions. At the outer edge of the cyclotron are carbon foils which, when impacted, strip off the electrons while allowing the heavier proton to pass through. The particle is now positively charged and will be bent out of the cyclotron and down one of the beamlines. Since the particle beam is still charged, it can be steered with magnets to a production target.

For the purpose of pion production a beryllium or carbon(graphite) target is used. The protons hit the production target and generates a pion, which then decays into a spin-polarized muon and a neutrino, as explained in Chapter 4. The muons are steered to one of four active beamlines, where they are passed through a Wien filter to separate out any positrons in the decay channel and where the desired muon momentum can also be selected by tuning the magnetic and electric fields using Equation (5.1). Surface muons are characterized by $p = 0.0289 \text{ GeV}/c$ and $\eta = 0.24$, so tuning the electric and magnetic fields so that $\epsilon/\eta = 300B$ means we should deflect the non-desirable particles out of the incident beam.

The muons are then focused further by quadrupole magnets, passed through a collimator and then reach the sample for implantation. Additionally, the separators are capable of creating a potential difference of 454 KeV, which can be used to rotate the spins by an angle ϕ , computed by Equation (5.2) so that measurements with spins oriented both along and transverse to the beam direction can be performed on the same sample.

$$\Delta\theta = \frac{d}{p} \left(\frac{\epsilon}{\eta} - 300B \right) \quad (5.1)$$

$$\phi = \frac{qBd}{\eta\Gamma} \quad (5.2)$$

where d is the length of the capacitor plates in m
 p is the particle momentum in GeV/c
 ϵ is the electric field gradient in MeV/m
 η is the relativistic speed parameter, v/c
 B is the magnetic field in Tesla
 γ is the relativistic Lorentz factor, $\frac{1}{\sqrt{1 - \eta^2}}$

Immediately prior to entering the sample, the muon passes through a scintillator, causing a detection that starts an electronic clock. At this point, if the muon passes through or misses the sample it will be incident on a second scintillator that will stop the clock and veto the event. Once the muon is incident with the sample, it loses kinetic energy by ionizing the outer shell electrons near its path, and it will eventually come to rest at an interstitial, or muon implantation, site. This process is not a magnetic interaction, and so this process has a negligible effect on the spin. The loss of kinetic energy takes, in general, less than one nanosecond. Typically, data is taken from the 10 ns mark (prior to this time any counts are considered background) out to $\sim 10 \mu s$, which is just over 4 muon half-lives. Only approximately 1 percent of muons would, based on decay statistics, not have decayed at this point in time.

The muon spin evolves based on the local magnetic field that it experiences. If the field is off axis, they will precess at their Larmor Frequency, which can be found in Table 4.1. If there are variations in position or time, for example from muon hopping or a dynamic relaxation, we would expect a dephasing or depolarization of the muons as well. Once the muon decays, the positron will be incident with another scintillator, causing a detection that stops the

electronic clock. This will then register a count in the appropriate statistical bin of the muon histogram.

5.1.1 LAMPF Instrument

For measurements above 2 K, the OMNI-LAMPF instrument at TRIUMF provides a good platform. It is comprised of three transverse Helmholtz coils which are capable of generating a magnetic field up to 4 kOe, or 0.4 T, by drawing 1 kA of current in the Meson Hall Annex, on beamline M15. It contains a set of forward/backward and up/down counters for creating both relevant transverse and longitudinal field histograms. For our experiment LAMPF was fit with a Quantum Design helium gas flow cryostat, which allows for a temperature range for the sample of between ~ 1.7 and 330 K. The sample was mounted on silver tape on a low background sample insert. Silver tape is used because implanted muons in the tape will have no relaxation, since silver is non-magnetic. An image of LAMPF fit with the gas cryostat is shown in Figure 5.1.

5.1.2 Dilution Refrigerator

For measurements below 2 K, an Oxford 400 dilution refrigerator was used. It has a base temperature of 10 mK, although it has been cooled to 8 mK and can be used as a normal cryostat for measurements up to 30 K. The spectrometer for the dilution refrigerator consists of a superconducting Helmholtz coil



Figure 5.1: The OMNI-LAMPF Instrument Fit with Gas Flow Cryostat (Image Courtesy of TRIUMF)

that is capable of generating a main field of up to 5 T, and also has secondary coils that can generate transverse fields of up to 5 mT.

Low temperature dilution refrigerators work using the properties of the isotopes of helium. When the two stable isotopes of helium, He^3 and He^4 , are cooled below a critical temperature they will separate into two phases, which are conventionally named by their concentration of the lighter isotope. The concentration of He^3 in each phase is temperature dependent. The enthalpy between the He^3 in the rich phase and the He^3 in the dilute phase are different as well, so when ‘evaporation’ of He^3 from the rich to the dilute phase occurs we get cooling. The He^4 comprising the bulk to the dilute phase is essentially

inert, as below 0.5 K He^4 is in its quantum mechanical ground state, and exhibits the properties of both a superfluid and a gas with zero spin. In the rich phase He^3 acts as an ideal Fermi gas, while in the dilute phase it moves through the He^4 as if the He^3 was in a vacuum due to quantum mechanics.

Initially, the 1K pot is used to condense the He^3/He^4 mixture down to 1.2 K. Cooling is provided by the still, where the incoming He^3 is cooled before it enters the heat exchangers and the mixing chamber. This cools the remainder of the dilution refrigerator to 0.86 K, where phase separation occurs. He^3 must be extracted continually from the dilute phase and returned to the rich phase in order to keep the dynamic equilibrium. This is done at the surface of the still, where He^3 evaporates at a rate that is several orders of magnitude faster than He^4 . The He^3 leaving the mixing chamber is used to cool the return flow of He^3 through the heat exchangers. A vacuum pumping system is used to remove the He^3 from the still and compress it before returning it through cold traps to the cryostat. It is then cooled by the main bath and condensed on the 1K pot[43]. An image of the dilution refrigerator and spectrometer are shown in Figure 5.2.

The sample holder used for this experiment in the dilution refrigerator was a flat silver finger mounted to the insert. The slices were aligned and mounted using Apiezon N grease and wrapped in silver foil. The silver foil was secured with a silver back plate and two screws to prevent any samples from falling into the dilution refrigerator.



Figure 5.2: The Oxford Dilution Refrigerator and Spectrometer (Image courtesy of Columbia University)

5.2 Transverse Field μ SR Experiments

Primarily, a series of measurements were performed at 50 mK in an array of fields from 500 G to 5 T. An insufficient amount of time resulted in insufficient data above 2 T to make reliable observations, as with such a high transverse field the number of implanted muons goes down drastically as the probability to miss the sample increases. These measurements were done in the dilution refrigerator. The most important result from this series of measurements was the confirmation of the long relaxation time as found by the heat capacity measurements. This is easily observed by comparing two runs, both done at 5 kG at 50 mK, separated in time by 12 hours. At the time of the first measurement the sample had been at 50 mK for over 13 hours. The second run was taken 12 hours after that. Both corrected asymmetry spectra, in the form of Equation (4.9) were analyzed and then Fourier transformed into frequency space. The expectation is that a signal from the silver sample holder will exist as a background signal. Silver is used because it has little effect on the muon. Silver is well characterized and has essentially no internal magnetism. The muon is expected to precess at its Larmor Frequency, 135.54 MHz/T. For 5 kG, or 0.5 T, we would expect a silver peak around 68 MHz. In this case that peak appears slightly closer to 69 MHz. The second signal we see is from the local magnetism at the muon site. The Fourier transform took the binned data from 0 to 5 μ s with a binning size of 0.2 ns. It was transformed with an expected peak of 69 MHz and with phase correction over the range 60 MHz to 78 MHz to prevent negative amplitudes. The fit was also strongly apodized to force the fit to smooth to zero at the edges of frequency space. The first run,

run 5121, is indicated in maroon in Figure 5.3. The second run, run 5126, is in black.

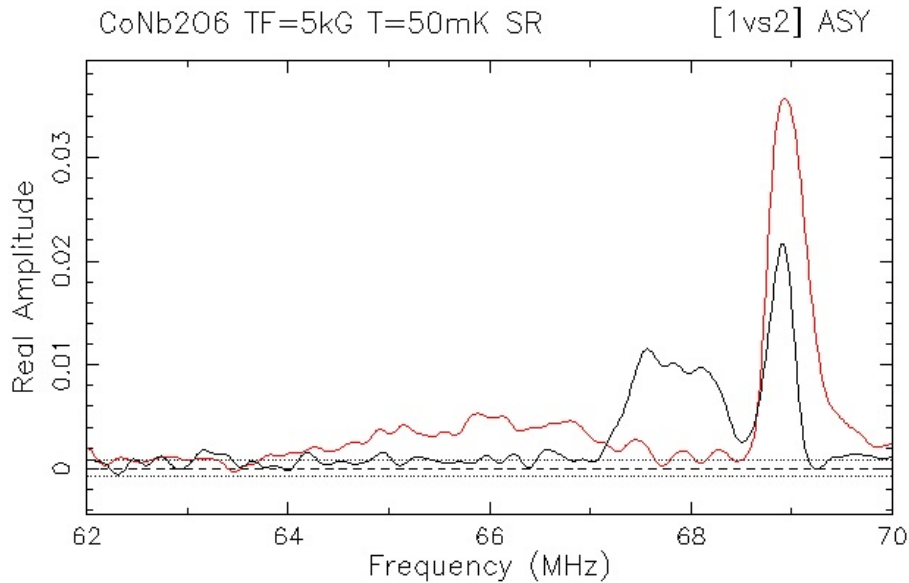


Figure 5.3: A plot of the Fourier transform for Run 5121 (Maroon Curve) and Run 5126 (Black Curve). These runs were taken at 50 mK at a transverse field strength of 5 kG after 13 and 25 hours of cooling.

From Figure 5.3, we see the silver peak as expected. In the first run there is a broad feature centred around 66 MHz which is coming from the sample itself. This is definitively shown when comparing the peaks to the data from the second run. The signal from the silver sample should remain static in position since its relaxation is essentially predetermined. We see that the signal coming from our sample has sharpened both in width and in height significantly. The second noticeable feature is that although the silver peak is located at the same location the spectral weight, or the area under the curve for that peak, has been reduced significantly. The frequency shift of the sample

peak implies that the system was not in thermal equilibrium after 13 hours, and even after an additional 12 hours it isn't possible to state that the data collected here is not in a thermally excited state.

This result confirms that the relaxation time for the system is exceptionally long; likely significantly longer than 13 hours at 50 mK. Unfortunately, control of the temperature was lost shortly after Run 5126 due to a blockage in the 1K pot, and the system warmed up by several hundred mK. Inadequate experimental time was available for further measurements of the settling of this material.

It appears the internal magnetic field is causing a fringing effect into the silver and enhancing the signal, and as the spins get closer to the ground state any sympathetic alignment seems to be drifting away from such an enhancement to the final ordered ground state of cobalt niobate.

5.3 Longitudinal and Zero Field μ SR Experiments

Longitudinal and zero field measurements were performed at a wide range of fields and temperatures. The field range probed was from zero field to 2 T, with the bulk of the measurements centred around 20 G and 500 G. At higher temperatures a switch from 20 G to 100 G was performed, as the thermal fluctuations at higher temperatures would be found to wash out or hide magnetic features, requiring a slightly stronger applied field. The temperature range probed was primarily from 700 mK through both phase transitions at 1.9 K and 2.9 K, up to 50 K in increasingly larger steps. In contrast to the

lowest temperatures probed using transverse fields, from the specific heat data we know the time constant and corresponding time required to ensure we are in thermal equilibrium, and we state that all the runs performed were done in such a state, or after the required amount of time.

The data was fit using the lowest temperature zero field data to determine a total asymmetry. Fits on each run were performed to determine the general trend, which was modelled as a stretched exponential. The general form of the stretched exponential is given in Equation (5.3)[33]. In the case of this material, dynamic relaxation is expected and so fitting to a stretched exponential makes actual sense.

$$G_z(t) = e^{-(\lambda t)^\zeta} \quad (5.3)$$

The values of ζ as a function of temperature are shown in Figure 5.4. Above 10 K there is a significant departure from a constant value. This is due to holding a fixed asymmetry when, in reality, the system dynamics are starting to change due to additional processes. It is normal to see a decrease in the exponent when approaching a phase transition. What we see is that below 2.9 K, the upper transition temperature, we get an asymmetry that can be fit linearly within error with these fields, which match the heat capacity data. The μ SR data is not precise enough to make a comparison to the change from a sharp to diffuse feature in heat capacity. The lowest temperature data fit was 700 mK. The value of ζ fits to an exponent of 0.78 ± 0.03 . Above the transition, up to ~ 8 K, ζ is constant as well with field, and has a value of 0.64 ± 0.02 other than for the 100 G case, which exhibits an additional decrease.

Based on the statistical errors computed by the fitting software, this may be due to constraints being modelled too tightly. The constraints chosen were kept uniform so that all the lowest temperature data could be modelled in an identical manner, assuming constant experimental parameters with respect to beam delivery, beam properties and equipment. When allowed to float, the individual values for the fixed parameters began to vary significantly above 2.5 K.

For the data in zero field, we see no evidence of oscillatory behaviour. The temperature dependence of the oscillation frequency of the polarization function in zero field is an order parameter in the ordered state. This type of behaviour is not exhibited by our data and therefore implies that the material itself is not ordered.

The stretched exponential is a phenomenological fit. Based on theoretical models, ζ would be expected to be either 1 at high temperatures, indicating a single dominating exponential relaxation, or $\frac{1}{2}$ in the case of a dilute magnetic system. When the value of ζ deviates from these values it generally indicates that spin dynamics have a significant role in determining the magnetism of the system, of which there are numerous potential origins. A deviation from or change in the ζ parameter generally indicates a spacial distribution of the muon fluctuation rates. In the case of a spin-glass, it is expected that near the transition temperature, T_g , the value of ζ should asymptotically approach $\frac{1}{3}$ [33].

The data was then fit both globally with respect to field, as well as individually for each run to determine the relaxation rate of the muons. The data

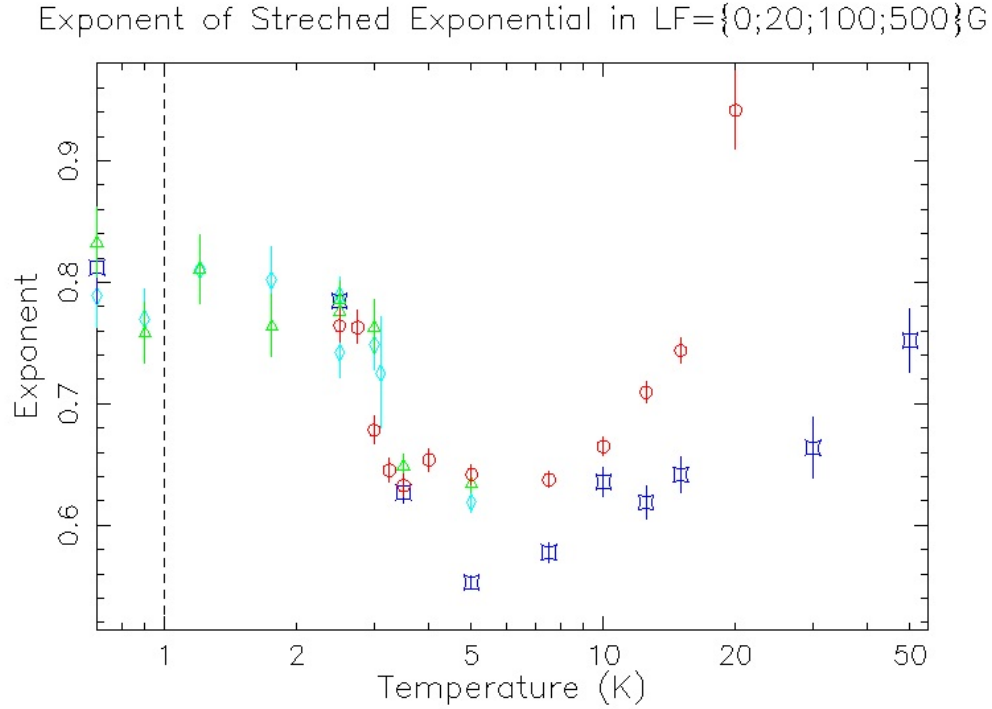


Figure 5.4: Values of ζ for zero field (Maroon) and longitudinal fields of 20 G (Green), 100 G (Blue) and 500 G (Light Blue)

is plotted in Figure 5.5. Below the upper transition at 2.9 K, we see that the relaxation rate becomes constant, indicative of magnetic ordering. Above the transition in the paramagnetic state we see the relaxation rate decreasing in an exponential fashion to zero, which is expected for a material in the paramagnetic state. The fact that the zero field and longitudinal field plots match both the relaxation rate and the power of the exponent so well is indicative of a lack of decoupling of this system at the fields measured. This gives an indication of the relative strength of the local magnetism within the material. Some data has been taken at higher fields, up to 2 T, and evidence of decoupling was seen. Higher statistics are required before a full explanation and measure

of the field strength required to decouple can be given. The changes seen to both the asymmetry plots with both an increase of field (Figure 5.7) and of temperature (Figure 5.8) indicate dynamic spin behaviour in this system. It should be noted that the application of a 20 G or 100 G longitudinal field simply act to decouple any nuclear dipole moment and do not have an effect on the dynamic relaxation. This is seen by comparing the zero field, 100 G and 500 G asymmetry fits from Figures 5.6 and 5.8.

In Figure 5.5 we do see a large change in relaxation rate around the transition temperature, but the plotted asymmetry functions do not seem to indicate static magnetism. We do notice that the field dependence of the relaxation rate at 5 K is larger than the relaxation rate below the transition. In an ordered state we would expect frozen magnetic moments, so we would expect the opposite trend in the field dependence.

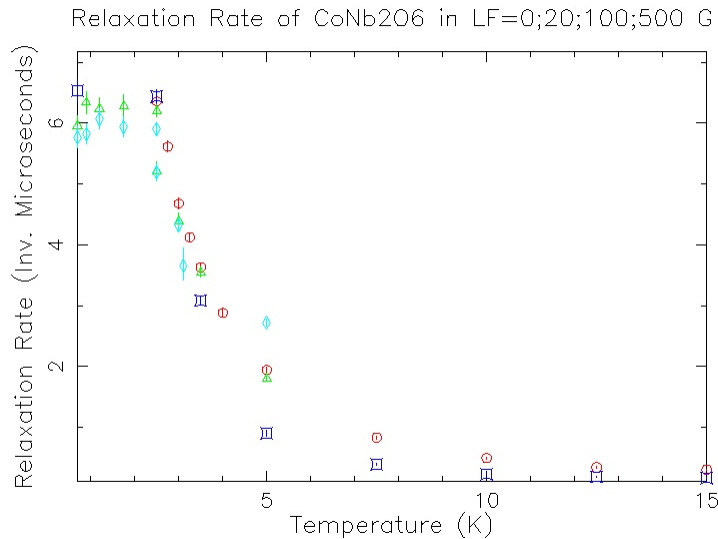


Figure 5.5: Values of Muon Relaxation Rate for Zero Field (Maroon) and Longitudinal Fields of 20 G (Green), 100 G (Blue) and 500 G (Light Blue)

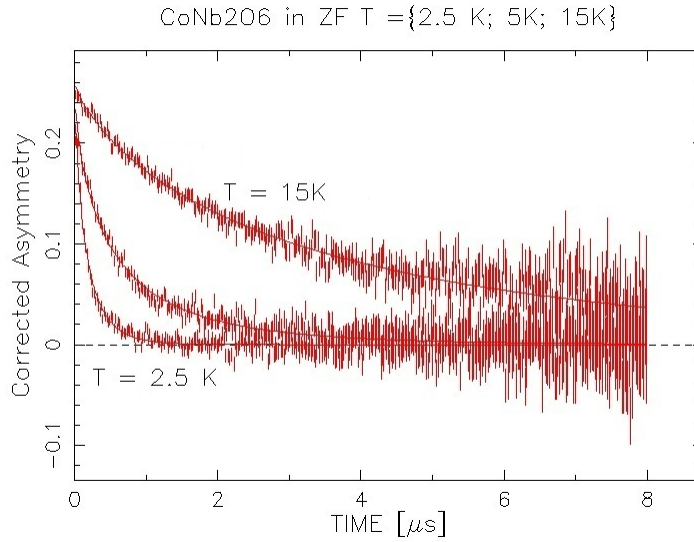


Figure 5.6: Cobalt Niobate Asymmetries in Zero Field at 2.5, 5 and 15 K in Order of Increasing Temperature

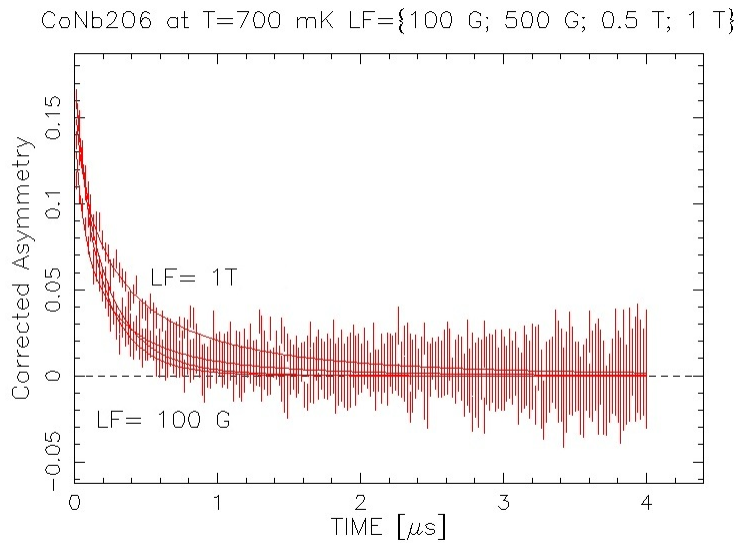


Figure 5.7: Cobalt Niobate Asymmetries at 700 mK with a Longitudinal Field of 100 G, 500 G, 0.5 T and 1 T in Order of Increasing Field

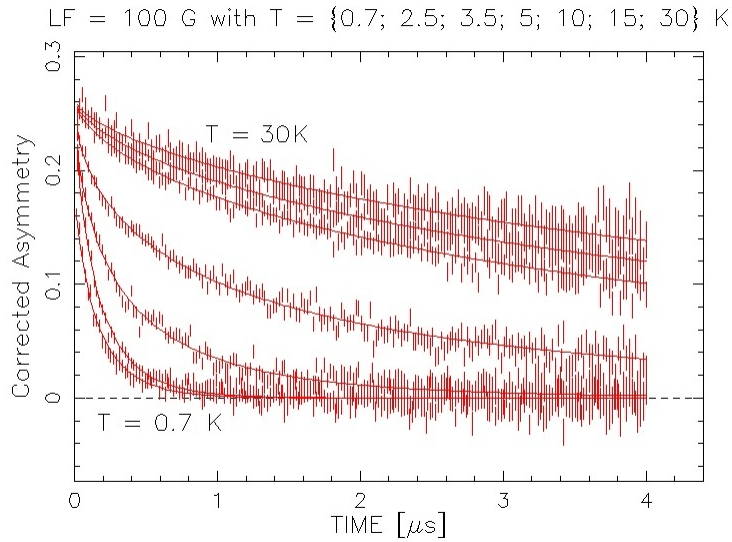


Figure 5.8: Cobalt Niobate Asymmetries in a Longitudinal Field of 100 G at 0.7 K, 2.5 K, 3.5 K, 5 K, 10 K, 15 K and 30 K in Order of Increasing Temperature

From the specific heat and the magnetic susceptibility data we see that there are phase transitions at 1.9 K and 2.9 K. From the μ SR data, however, we see very dynamic behaviour within the system. In fact, μ SR does not actually show any real evidence for a magnetically ordered state on the time scales probed. We would expect to see large features, particularly at the presumed transition temperatures. Since these features on the bulk scale are not seen at the microscopic scale, it can be inferred that the transitions we see are not due to a long range ordered state. The low temperature states must still have a large dynamic nature so that they can still cause the muons to relax. Some evidence of this dynamic behaviour may be being reflected in the long time constants found in the specific heat measurements.

Chapter 6

Conclusions

Cobalt niobate, CoNb_2O_6 , is an interesting example of a real substance that acts closely to a predicted theoretical model. This material was successfully synthesized and grown at McMaster University using the optical floating zone technique. The material required a fast pre-melt phase to increase rod density before a successful, slow growth could be performed to create a high-quality single crystal sample. The material synthesis was confirmed with powder and single crystal x-ray diffraction and crystal alignment was performed using Laue x-ray diffraction on the outer surface as well as on the cut crystal face.

Using SQUID magnetometry, magnetic susceptibility measurements showed that the crystal reproduced peaks matching the literature values and additionally confirmed that crystal orientation with respect to applied field plays a large role in the overall magnetic characteristics expressed by this material.

Heat capacity measurements were performed at temperatures above 2 K in several field ranges, and were able to detect the expected magnetic phase transition to a magnetically-ordered state. It was also found that the application of a small field changed the heat capacity peak from a sharp feature to a more

diffuse feature. Future work will look at exactly how small a field is required to cause the smoothing of this peak, and also look at higher applied fields. Measurements were also taken below 1 K with the goal of extending the known data below previous values, which had only been taken to 0.5 K. At present, measurements have been done down to 0.33 K, and the care taken in these measurements has shown a significant departure from what was previously known. The specific heat and corresponding relaxation time constant were found to increase in an exponential manner. This suggests that experiments done in this regime need to be done with due regard for the relaxation time if the ground state in thermal equilibrium is to be fully determined. Further studies below 0.3 K as well as with an applied field need to be performed to extend the known phase diagram, and to confirm the behaviour seen in recent neutron studies, as referenced in Chapter 1.

μ SR studies were also undertaken at low temperature in fields from 0 to 2 T. The transverse field results confirm that there is a very long relaxation time exhibited by this material. There seems to be only a single muon site, as the transverse field shows a broad peak in frequency space other than the known sample holder, but it should be noted that this peak shifts and sharpens with increased settling time. When the time constant for very low temperatures is better known, revisiting these measurements will likely provide a far better picture on the local magnetism expressed in this material. Zero field and longitudinal field measurements confirm the magnetic ordering from paramagnetic to a new state at 2.9 K as expected by previous phase diagrams, with a muon relaxation rate of $\sim 6 \text{ ms}^{-1}$ and a value of $\beta=0.78$ as a value for the exponent of the stretched exponential fit, which is a departure from $\beta=0.65$ found

above the transition. The behaviour we see in the asymmetry spectra is highly dynamic in nature, and conclusive evidence of decoupling of the internal and external fields in the longitudinal orientation has not yet been seen, indicating this material has strong internal moments. Of particular interest is that, in the regime surveyed, μ SR shows no sign of a statically ordered state, and no large features in the asymmetry spectra at the transition temperatures of 1.9 K and 2.9 K.

Bibliography

- [1] H. Weitzel. Kristallstrukturverfeinerung von Wolframiten und Columbiten. *Zeitschrift für Kristallographie*, 144(1-6):238–258, 1976.
- [2] R. Coldea, D. A. Tennant, E. M. Wheeler, E. Wawrzynska, D. Prabhakaran, M. Telling, K. Habicht, P. Smeibidl, and K. Kiefer. Quantum criticality in an Ising chain: experimental evidence for emergent E8 symmetry. *Science*, 327(5962):177–180, 2010.
- [3] T. Hanawa, K. Shinkawa, M. Ishikawa, K. Miyatani, K. Saito, and K. Kohn. Anisotropic specific heat of CoNb₂O₆ in magnetic fields. *Journal of the Physical Society of Japan*, 63(7):2706–2715, 1994.
- [4] S. Kobayashi, S. Mitsuda, T. Jogetsu, J. Miyamoto, H. Katagiri, and K. Kohn. Anisotropic growth kinetics in the geometrically frustrated isosceles triangular Ising antiferromagnet CoNb₂O₆. *Physical Review B*, 60(14):9908–9911, 1999.
- [5] P. W. C Sarvezuk, E. J. Kinast, C. V. Colin, M. A. Gusmão, J. B. M. da Cunha, and O. Isnard. New investigation of the magnetic structure of CoNb₂O₆ columbite. *Journal of Applied Physics*, 109:07E160, 2011.
- [6] S. Mitsuda, K. Hosoya, T. Wada, H. Yoshizawa, T. Hanawa, M. Ishikawa, K. Miyatani, K. Saito, and K. Kohn. Magnetic ordering in one-

- dimensional system CoNb₂O₆ with competing interchain interactions. *Journal of the Physical Society of Japan*, 63(10):3568–3571, 1994.
- [7] I. Maartense, I. Yaeger, and B.M. Wanklyn. Field-induced magnetic transitions of CoNb₂O₆ in the ordered state. *Solid State Communications*, 21(1):93 – 96, 1977.
- [8] W. Scharf, H. Weitzel, I. Yaeger, I. Maartense, and B. M. Wanklyn. Magnetic structures of CoNb₂O₆. *Journal of Magnetism and Magnetic Materials*, 13(1-2):121–124, 1979.
- [9] Takeshi Hanawa, Masayasu Ishikawa, and Kazuo Miyatani. Disappearance of Ferromagnetism at Low Temperatures in CoNb₂O₆. *Journal of the Physical Society of Japan*, 61(12):4287–4289, 1992.
- [10] C. Kittel. *Introduction to solid state physics*. Wiley, 1996.
- [11] C. Heid, H. Weitzel, P. Burlet, M. Bonnet, W. Gonschorek, T. Vogt, J. Norwig, and H. Fuess. Magnetic phase diagram of CoNb₂O₆: A neutron diffraction study. *Journal of magnetism and magnetic materials*, 151(1):123–131, 1995.
- [12] C. Heid, H. Weitzel, P. Burlet, M. Winkelmann, H. Ehrenberg, and H. Fuess. Magnetic phase diagrams of CoNb₂O₆. *Physica B: Condensed Matter*, 234:574–575, 1997.
- [13] A.B. Zamolodchikov. Integrals of motion and S-matrix of the (scaled) T=T_c Ising model with magnetic field. *International Journal of Modern Physics A*, 4(16):4235–4248, 1989.

- [14] S.B. Lee, R.K. Kaul, and L. Balents. Interplay of quantum criticality and geometric frustration in columbite. *Nature Physics*, 6(9):702–706, 2010.
- [15] H. A. Dabkowska and A. B. Dabkowski. Crystal Growth of Oxides by Optical Floating Zone Technique. In Govindhan Dhanaraj, Kulliah Byrappa, Vishwanath Prasad, and Michael Dudley, editors, *Springer Handbook of Crystal Growth*, pages 367–391. Springer Berlin Heidelberg, 2010.
- [16] C. Marjerrison, H. A. Dabkowska, A. B. Dabkowski, J. Greedan, G. M. Luke, and B. D. Gaulin. Growth of Multiple Valencies of Vanadate Systems. 2012.
- [17] B. D. Gaulin. Conference Summary and Conclusion. Presented as the Conference Summary and Conclusion, 2012.
- [18] N. W. Ashcroft and N. D. Mermin. *Solid State Physics*. Saunders College Publishing, 1976.
- [19] M. T. Dove. *Structure and Dynamics: An Atomic View of Materials*. Oxford Master Series in Condensed Matter Physics. Oxford University Press, USA, 2003.
- [20] S.T. Thornton and A. Rex. *Modern Physics for Scientists and Engineers*. Cengage Learning, 2012.
- [21] B. D. Cullity and S. R. Stock. *Elements of x-ray diffraction*. Pearson education. Prentice Hall, 2001.

- [22] R. R. Neurgaonkar and W. K. Cory. Progress in photorefractive tungsten bronze crystals. *Journal of the Optical Society of America B Optical Physics*, 3:274–282, Feb 1986.
- [23] T. J. S. Munsie, G. M. Luke, and H. A. Dabkowska. Investigation of Single Crystal Holmium Titanate Grown under Changing Conditions by the Optical Floating Zone Method.
- [24] H. Czichos, T. Saito, and L. Smith. *Springer Handbook of Materials Measurement Methods*. Number v. 978, nos. 3-20786 in Springer handbooks. Springer, 2006.
- [25] D. Prabhakaran, F. R. Wondre, and A. T. Boothroyd. Preparation of large single crystals of ANb₂O₆ (A=Ni, Co, Fe, Mn) by the floating-zone method. *Journal of Crystal Growth*, 250(12):72–76, 2003. Proceedings of the Fourteenth American Conference on Crystal Growth and Epitaxy.
- [26] D. Pomaranski and J. Kycia. Low Temperature Specific Heat Measurements of Frustrated Magnetic Materials. *Physics in Canada*, 68(2), 2012.
- [27] D. Scalbert, J. Cernogora, and C. Benoit A La Guillaume. Spin-lattice relaxation in paramagnetic CdMnTe. *Solid State Communications*, 66(6):571 – 574, 1988.
- [28] C. Kittel and H. Kroemer. *Thermal Physics*. W. H. Freeman, 1980.
- [29] R. Alfaro, E. Belmont-Moreno, A. Cervantes, V. Grabski, JM López-Robles, L. Manzanilla, A. Martinez-Davalos, M. Moreno, and

- A. Menchaca-Rocha. A muon detector to be installed at the Pyramid of the Sun. *Revista mexicana de física*, 49:54–59, 2003.
- [30] D. Griffiths. *Introduction to Elementary Particles*. Physics Textbook. John Wiley & Sons, 2008.
- [31] J. Beringer et al. Review of Particle Physics (RPP). *Phys.Rev.*, D86:010001, 2012.
- [32] Peter J. Mohr, Barry N. Taylor, and David B. Newell. CODATA Recommended Values of the Fundamental Physical Constants: 2010, 2012.
- [33] S.L. Lee, R. Cywinski, and S.H. Kilcoyne. *Muon Science: Muons in Physics, Chemistry and Materials*. Scottish universities summer school. Taylor & Francis, 1999.
- [34] Spring School on Muon Spin Research, J. Chappert, R.I. Grynszpan, and Centre national de la recherche scientifique (France). *Muons and pions in materials research: lectures delivered at the Spring School on Muon Spin Research, Aussois, France, May 1983*. North Holland, 1984.
- [35] J.E. Sonier. Muon Spin Rotation/Relaxation/Resonance (μ SR). TRI-UMF Brochure, April 2002.
- [36] J.E. Sonier. *The Magnetic Penetration Depth of the Vortex Core Radius in Type-II Superconductors*. PhD thesis, University of British Columbia, 1998.
- [37] S.F.J. Cox. Implanted muon studies in condensed matter science. *Journal of Physics C: Solid State Physics*, 20(22):3187, 2000.

- [38] M.T. Rovers. Spin Liquid Behaviour in Geometrically Frustrated Chromium Oxides. Master's thesis, McMaster University, 2001.
- [39] A. DeVisser. Muon Spin Rotation/Relaxation/Resonance, 2004. Lecture at Universiteit van Amsterdam.
- [40] S.J. Blundell. Muon Relaxation Functions, 2008. Lecture to the 2008 ISIS Muon Training Course.
- [41] B. Cywinski. Muon Spin Relaxation Functions, 2005. Lecture to the 2005 ISIS Muon Training Course.
- [42] P.D. De Reotier and A. Yaouanc. Muon spin rotation and relaxation in magnetic materials. *arXiv preprint cond-mat/9710235*, 1997.
- [43] N. Craig and T. Lester. Hitchhikers Guide to the Dilution Refrigerator, August 2004. Marcus Lab, Harvard University.